Spatio-Spectral Color Filter Array Design for Optimal Image Recovery

Keigo Hirakawa, *Member, IEEE*, and Patrick J. Wolfe, *Senior Member, IEEE*

***Abstract*—In digital imaging applications, data are typically obtained via a spatial subsampling procedure implemented as a color filter array—a physical construction whereby only a single color value is measured at each pixel location. Owing to the growing ubiquity of color imaging and display devices, much recent work has focused on the implications of such arrays for subsequent digital processing, including in particular the canonical *demosaicking* task of reconstructing a full color image from spatially subsampled and incomplete color data acquired under a particular choice of array pattern. In contrast to the majority of the demosaicking literature, we consider here the problem of color filter array *design* and its implications for spatial reconstruction quality. We pose this problem formally as one of simultaneously maximizing the spectral radii of luminance and chrominance channels subject to perfect reconstruction, and—after proving sub-optimality of a wide class of existing array patterns—provide a constructive method for its solution that yields robust, new panchromatic designs implementable as subtractive colors. Empirical evaluations on multiple color image test sets support our theoretical results, and indicate the potential of these patterns to increase spatial resolution for fixed sensor size, and to contribute to improved reconstruction fidelity as well as significantly reduced hardware complexity.**

***Index Terms*—Color filter array (CFA), color imaging, demosaicking, digital camera pipeline, spatio-spectral sampling.**

I. Introduction

Owing to the growing ubiquity of color imaging devices, much recent work has focused on the interplay between their acquisition stages and subsequent digital processing. In most applications, data are obtained via a subsampling procedure implemented as a color filter array (CFA), a physical construction whereby each pixel location measures only a portion of the visible spectrum, selected from amongst a chosen "color partition" of that spectrum—typically corresponding to long, medium, and short wavelengths—which in turn induces a spatial sampling pattern for each such color representative. This array represents one of the first steps in the acquisition pipeline, and, hence, CFA design determines to a great extent the maximal resolution achievable by subsequent processing schemes. These schemes typically assume a full-color image (i.e., a full set of color triples), and consequently, a key reconstruction task termed *demosaicking* is first necessary. This refers to the inverse problem of reconstructing a spatially undersampled set whose components correspond to particular tristimulus values—typically red, green, and blue.

In this paper we address the problem of color filter array design and its implications for spatial reconstruction quality. Our aim is to rigorously quantify the attainable limits of CFA performance, while at the same time providing a framework that both identifies the fundamental limitations of existing designs and explains the performance of well-known associated demosaicking approaches appearing in the literature. As we detail in this paper, the inherent shortcomings of contemporary CFA designs mean that subsequent processing and reconstruction steps often yield diminishing returns. Indeed, the loss of image quality resulting from all but the most computationally expensive state-of-the-art methods is unambiguously apparent to the practiced eye.

We pose the CFA design problem formally as one of simultaneously maximizing the spectral radii of luminance and chrominance channels subject to perfect reconstruction. In doing so we unify several recent approaches in the literature, including most notably the use of Fourier analysis as a tool to view demosaicking as "demultiplexing" [2], [3], and the notion of reconstruction based on chrominance/luminance decompositions [4]–[6]. Under this formulation, we demonstrate the surprising result of sub-optimality of designs based on "pure" tristimulus values, a class that includes the well-known Bayer pattern currently most popular in industry. As an alternative, we provide a constructive method to generate feasible CFA designs that have been optimized for additional design metrics.

The additional criteria we consider are quality of reconstruction, complexity of implementation, quantum efficiency and noise, and robustness to prior assumptions on color channel bandlimitedness. As our emphasis is on improving the color image acquisition pipeline rather than on developing optimal demosaicking strategies per se, we omit a comparative analysis of reconstruction techniques; however, our results yield a general class of linear demosaicking methods that provide state-of-the-art performance and are demonstrably robust to spatio-chromatic aliasing. In addition to reducing hardware complexity relative to the nonlinear demosaicking techniques that currently predominate, it can be expected that these linear methods will also enable more tractable noise modeling [7].

The remainder of this paper is organized as follows. We begin in Section II by analyzing the spatio-spectral properties of typical color images and the Fourier representations that lattice-structured CFA samplings induce, in order to demonstrate sub-

Manuscript received October 26, 2007; revised May 4, 2008. Current version published September 10, 2008. Patent pending. Preliminary results first appeared in the 2007 IEEE International Conference on Image Processing (ICIP). This work was supported in part by the National Science Foundation under Grant DMS-0652743. The associate editor coordinating the review of this manuscript and approving it for publication was Dr. Ricardo L. de Queiroz.

The authors are with the Statistics and Information Sciences Laboratory, Harvard University, Cambridge, MA 02138 USA (e-mail: hirakawa@stat.harvard.edu; patrick@seas.harvard.edu).

Color versions of one or more of the figures in this paper are available online at http://ieeexplore.ieee.org.

Digital Object Identifier 10.1109/TIP.2008.2002164

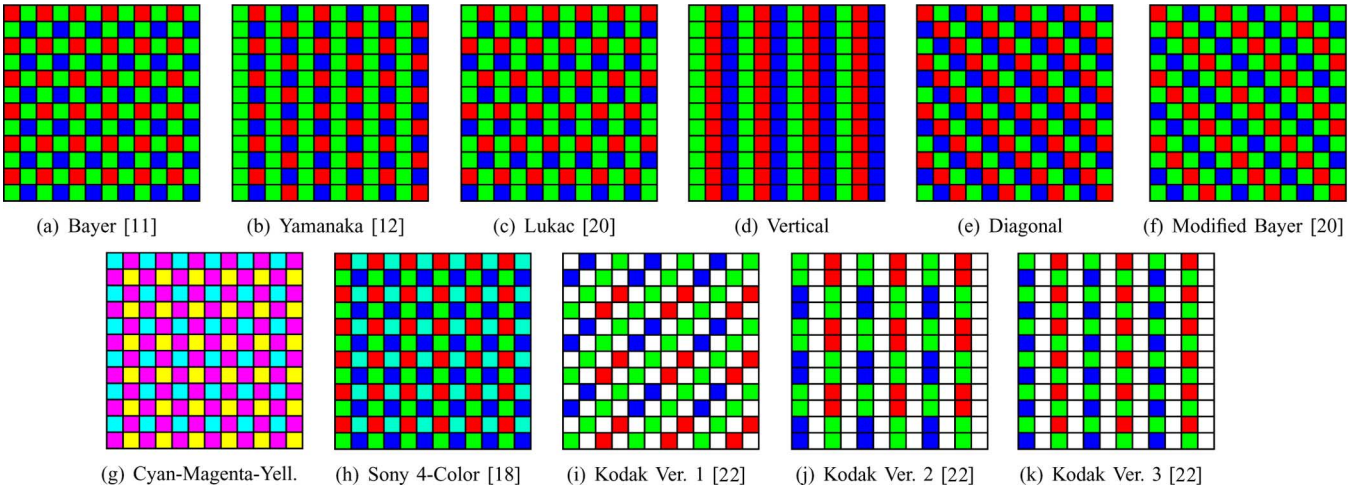

Fig. 1. Examples of existing color filter array patterns, with pure-color designs shown along the top row and panchromatic designs along the bottom.

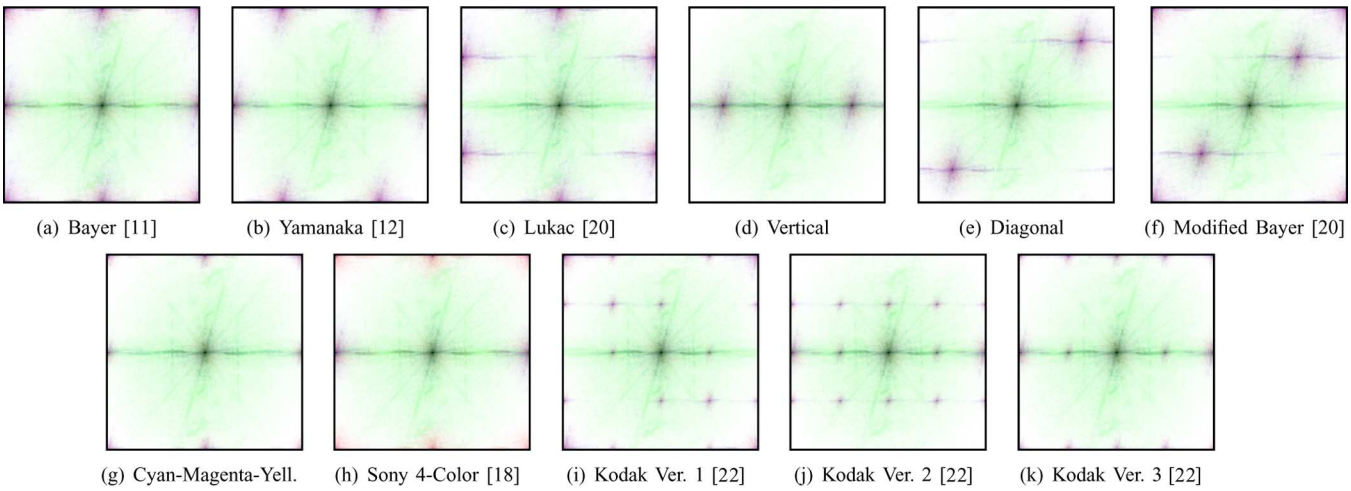

Fig. 2. Log-magnitude spectra of respective sensor data representing the "lighthouse" image [4]. Figures are color-coded: $\mathrm{green} = X_g, \mathrm{red} = X_\alpha, \mathrm{blue} = X_\beta$, with intensity reflecting relative weights assigned to modulated spectral replicates according to the geometry of the color filter array in question.

optimality of existing CFA designs. (Though requisite tools and vocabulary will be provided, this section may be safely skipped by readers unfamiliar with lattice theory.) We propose in Section III a constructive framework for designing and analyzing alternative patterns that simultaneously minimize aliasing and admit fast, optimal linear reconstruction schemes. In Section IV, we provide several explicit examples of new patterns whose closed-form expressions are directly realizable as so-called subtractive colors, and provide evaluations on standard image test sets. We summarize our results and conclude with a brief discussion in Section V.

II. Analysis: Existing Patterns and Algorithms

We first proceed to analyze the spatio-spectral sampling induced by a typical CFA pattern, which we model as a spatial array of pixel sensors. As alluded to earlier, a physical device termed a *color filter* rests over the photosensitive element at each pixel location; it passes a certain portion of the visible spectrum of light according to its chemical composition. The resultant measurement may be considered as an inner product resulting from a spatiotemporal integration of the incident light over each pixel's physical area and exposure time, taken with respect to the color filter's spectral response. While this *spectral response* is an intrinsic property of the filter, its perceived *color* is in fact a function of the environmental illuminant; however, here we adopt the standard convention and identify the filters typically used in practice by their "colors" as red, green, and blue. Our later analysis will rely on convex combinations of these components as "pure-color" building blocks, the precise spectral response of which is left to the designer [8].[1] As the goal of this paper is the identification and optimization of relevant *objective* metrics, rather than *subjective* metrics related to perception, we make no further attempt to treat issues of color science.

In a typical acquisition scenario, a regular, repeating CFA pattern comprises a tiling of the image plane formed by the union of interleaved sets of sampling, which in turn may be understood

[1]Ideally, one would design the spectral response of such pure-color filters by experimentally optimizing over the range of illuminants typically seen in practice [9]; however, such considerations are beyond the scope of our present discussion. Moreover, other issues such as dye chemistry, quality control, prior art, etc. arise in an industry setting, and may be equally important in practice.

in terms of lattices [10]; the spectral periodicity of the resultant sampled color image is determined by a so-called dual lattice, thereby enabling us to characterize the effect on individual color channels of the spatio-spectral sampling induced by various CFA patterns. By explicitly considering this spatio-spectral representation, we are able both to quantify the fundamental limitations of existing CFA designs as evidenced through their associated demosaicking algorithms, and to explicitly demonstrate the sub-optimality of a class of designs that includes most CFA patterns currently in wide use.

A. Spatio-Spectral Analysis of Sensor Data

The well-known Bayer pattern CFA [11], illustrated in Fig. 1(a), attempts to complement humans' spatial color sensitivity via a quincunx sampling of the green component that is twice as dense as that of red and blue. Though the Bayer pattern remains the industry standard, a variety of alternative color schemes and geometries have been considered over the years [8], [12]–[21], certain of which are also shown in Fig. 1. In order to understand the shortcomings and limitations associated with the state of the art in color filter array design and demosaicking, it is necessary to consider the *geometric* structure of color filter arrays as well as the *algebraic* structure of the sampling patterns they induce—examples of which are shown in Fig. 2. The requisite tools and vocabulary for this task will be provided by the notion of point lattices, the basics of which we discuss briefly below (using the notation of [10]).

1) Point Lattices as Sampling Sets: We will employ the notion of lattices to describe the spatial subsampling induced by CFA patterns. Indeed, lattices are central to the idea of "structured sampling" in Euclidean space, as they capture in greatest group-theoretic generality the notion of separated, yet regular, measurement points. Formally, a uniform lattice $\Lambda \subset \mathbb{R}^n$ comprises a discrete subgroup of n-dimensional Euclidean space whose quotient is compact. We say a nonsingular matrix $\boldsymbol{M}$ having real entries *generates* a point lattice $\Lambda_{\boldsymbol{M}}$ if $\Lambda_{\boldsymbol{M}} = \boldsymbol{M}\mathbb{Z}^n$, in which case columns of $\boldsymbol{M}$ are said to form a basis for the lattice. In the engineering literature $\boldsymbol{M}$ is often called a *sampling matrix*, as it generates a periodic measurement pattern indexed by n-tuples of integers precisely according to the lattice $\Lambda_{\boldsymbol{M}}$. We associate with each lattice $\Lambda_{\boldsymbol{M}}$ a quantity $\mathrm{vol}(\Lambda_{\boldsymbol{M}}) := |\det(\boldsymbol{M})|$ that generalizes the notion of a sampling period and is independent of the lattice basis.

As our main interest here lies in lattices as models for color filter arrays, we focus on the unit-volume square lattice $\mathbb{Z}^2$ as the setting for our image sensor—though our subsequent results apply equally well to other settings such as octagonal [15] or hexagonal [16] sensor geometries. The associated color sampling patterns may then be represented by less dense lattices, said to be sublattices[2] of $\mathbb{Z}^2$ if each of their elements also belongs to $\mathbb{Z}^2$. The volume of a sublattice $\Lambda_{\boldsymbol{M}} \subset \mathbb{Z}^2$ is consequently integer-valued, and no less than $\mathrm{vol}(\mathbb{Z}^2) = 1$.

A key point is that $\mathbb{Z}^2$ can be written as a disjoint union of *distinct translates* of a given sublattice $\Lambda_{\boldsymbol{M}}$—whereupon such translates can be associated with a red, green, or blue pure-color filter. The set of distinct translates of $\Lambda_{\boldsymbol{M}}$ by vectors in $\mathbb{Z}^2$ is said to form a set of *cosets* of $\Lambda_{\boldsymbol{M}}$ in $\mathbb{Z}^2$, with the corresponding vectors termed coset vectors. The number of distinct coset vectors (including the zero vector)—and, hence, disjoint translates—of such a sublattice is given by $\mathrm{vol}(\Lambda_{\boldsymbol{M}})$. Note that if we specify a regular, repeating pure-color CFA pattern based on the sublattice $\Lambda_{\boldsymbol{M}} \subset \mathbb{Z}^2$, then the number of different colors it admits cannot exceed the number of distinct cosets in $\mathrm{vol}(\Lambda_{\boldsymbol{M}})$. To this end, we call a sampling matrix $\boldsymbol{M}$ *admissible* if it generates a sublattice $\Lambda_{\boldsymbol{M}} \subset \mathbb{Z}^2$ with $\mathrm{vol}(\Lambda_{\boldsymbol{M}}) \geq 3$, and henceforth consider admissible generators.

2) A Lattice Model for Color Filter Arrays: Our goal is first to analyze pure-color CFAs comprising disjoint sampling patterns of red, green, and blue. To this end, recall that in a single-sensor camera, a scalar measurement is made at each spatial location $\boldsymbol{n} \in \mathbb{Z}^2$, leading to an idealized, noise-free model in which the sensor measurement $y(\boldsymbol{n})$ can be expressed as the inner product of the true color image triple $\boldsymbol{x}(\boldsymbol{n}) := [x_r(\boldsymbol{n}), x_g(\boldsymbol{n}), x_b(\boldsymbol{n})]^T$ and the action of the CFA $\boldsymbol{c}(\boldsymbol{n}) := [c_r(\boldsymbol{n}), c_g(\boldsymbol{n}), c_b(\boldsymbol{n})]^T$ as follows:

$$y(\boldsymbol{n}) = \boldsymbol{c}(\boldsymbol{n})^T \boldsymbol{x}(\boldsymbol{n}), \quad \boldsymbol{n} \in \mathbb{Z}^2. \tag{1}$$

Recall that by our description, a pure-color CFA $\{\boldsymbol{c}(\boldsymbol{n}) : \boldsymbol{n} \in \mathbb{Z}^2\}$ comprises a regular, repeating pattern that measures only a *single* component of the color triple at each spatial location, and, hence, its elements are represented by the standard basis.

Our model for the geometry of a pure-color CFA will thus be a vector-valued indicator function expressed in the language of lattices. We wish to partition $\mathbb{Z}^2$ into three structured sampling sets, each of which will be written as a union of selected cosets of a given sublattice $\Lambda_{\boldsymbol{M}} \subset \mathbb{Z}^2$. Sampling structures of this nature have been the subject of much previous study [10]; here we employ this notion to account for the color triple associated with each pixel, as described earlier. To this end, let $\boldsymbol{M}$ denote an admissible generator for sublattice $\Lambda_{\boldsymbol{M}} \subset \mathbb{Z}^2$ and let Ψ_r, Ψ_g, Ψ_b represent mutually exclusive subsets of coset vectors associated respectively with the spatial sampling locations of colors red, green, and blue.

If $\mathbb{Z}^2$ can be written as the disjoint union of the three interleaved sampling structures $\Psi_r + \Lambda_{\boldsymbol{M}}$, $\Psi_g + \Lambda_{\boldsymbol{M}}$, and $\Psi_b + \Lambda_{\boldsymbol{M}}$, each one comprising a union of selected cosets as $\{\Psi + \Lambda_{\boldsymbol{M}}\} := \cup_{\boldsymbol{\psi} \in \Psi}\{\boldsymbol{\psi} + \Lambda_{\boldsymbol{M}}\}$, then we call the result a *3-partition* of $\mathbb{Z}^2$. Note that, since under this scenario every sensor measures exactly one color, it suffices to specify $(\boldsymbol{M}, \Psi_r, \Psi_b)$, from which we can obtain the coset vectors Ψ_g accordingly. We subsequently adopt this description and exploit it in a luminance/chrominance parameterization below.

We take a given 3-partition of $\mathbb{Z}^2$ to be our model for pure-color sampling, in contrast to the new panchromatic CFA designs we introduce later, whose quantum efficiency functions have broader sensitivities. The sampling structure of the pure-color CFA associated with 3-partition $(\boldsymbol{M}, \Psi_r, \Psi_b)$ is then defined pointwise as follows:

$$\boldsymbol{c}(\boldsymbol{n}) = \begin{bmatrix} c_r(\boldsymbol{n}) \\ c_g(\boldsymbol{n}) \\ c_b(\boldsymbol{n}) \end{bmatrix} = \begin{bmatrix} \sum_{\boldsymbol{n_o} \in \{\Psi_r + \Lambda_{\boldsymbol{M}}\}} \delta(\boldsymbol{n} - \boldsymbol{n_o}) \\ \sum_{\boldsymbol{n_o} \in \{\Psi_g + \Lambda_{\boldsymbol{M}}\}} \delta(\boldsymbol{n} - \boldsymbol{n_o}) \\ \sum_{\boldsymbol{n_o} \in \{\Psi_b + \Lambda_{\boldsymbol{M}}\}} \delta(\boldsymbol{n} - \boldsymbol{n_o}) \end{bmatrix} \tag{2}$$

[2]Example sublattices of $\mathbb{Z}^2$ include the square sublattice generated by $\boldsymbol{M} = \begin{bmatrix} 2 & 0 \\ 0 & 2 \end{bmatrix}$, and the quincunx sublattice generated by $\boldsymbol{M} = \begin{bmatrix} 1 & 1 \\ -1 & 1 \end{bmatrix}$.

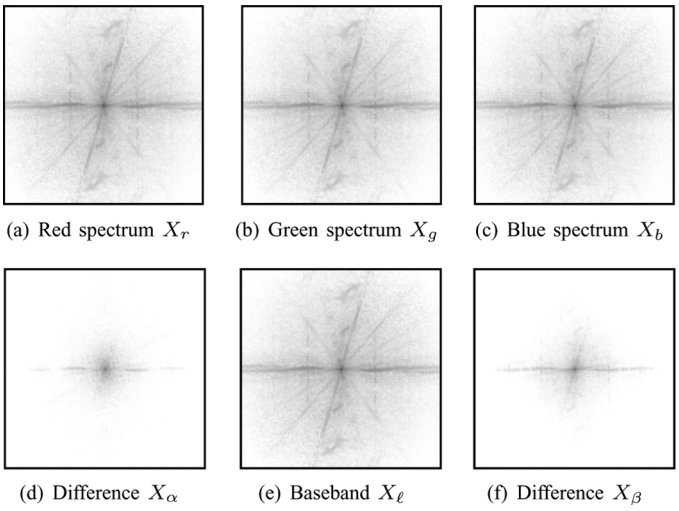

(a) Red spectrum X_r (b) Green spectrum X_g (c) Blue spectrum X_b

(d) Difference X_α (e) Baseband X_ℓ (f) Difference X_β

Fig. 3. Log-magnitude spectra of color channels of the "lighthouse" image, showing the contrast in bandwidth between the (x_r, x_g, x_b) representation of interest and a chrominance/luminance representation in terms of $(x_\alpha, x_\ell, x_\beta)$.

where by slight abuse of notation we let $\delta(\cdot)$ denote the Dirac or Kronecker delta function, as indicated by sampling context.

Pure-color CFAs hence perform a spatio-chromatic subsampling that effectively multiplexes red, blue, and green components in the spatial frequency domain—leading to the image recovery task known as demosaicking. However, because the spatio-spectral content of these color channels tends to be correlated at high spatial frequencies [4], [23], representations that exploit this correlation are often employed in contemporary demosaicking algorithms [20]. Here, we exploit a luminance/chrominance representation common in the literature to simplify our lattice model for pure-color CFAs. Following the measurement model of (1), each pixel sensor measurement may equivalently be represented in terms of a green channel x_g and difference channels $x_\alpha := x_r - x_g$ and $x_\beta := x_b - x_g$

$$\begin{aligned} y(\boldsymbol{n}) &= \boldsymbol{c}(\boldsymbol{n})^T \boldsymbol{I} \boldsymbol{x}(\boldsymbol{n}) \\ &= \boldsymbol{c}(\boldsymbol{n})^T \begin{bmatrix} 1 & 1 & 0 \\ 0 & 1 & 0 \\ 0 & 1 & 1 \end{bmatrix} \begin{bmatrix} 1 & -1 & 0 \\ 0 & 1 & 0 \\ 0 & -1 & 1 \end{bmatrix} \boldsymbol{x}(\boldsymbol{n}) \\ &= \begin{bmatrix} c_r(\boldsymbol{n}) & 1 & c_b(\boldsymbol{n}) \end{bmatrix} \begin{bmatrix} x_\alpha(\boldsymbol{n}) \\ x_g(\boldsymbol{n}) \\ x_\beta(\boldsymbol{n}) \end{bmatrix}. \end{aligned} \tag{3}$$

The advantage of this representation, as noted by [2] and [3], is that these difference channels enjoy rapid spectral decay—see Fig. 3—and can serve as a proxy for chrominance, whereas the green channel can be taken to represent luminance. As our eventual image recovery task will be to approximate the true color image triple $\boldsymbol{x}(\boldsymbol{n})$ from acquired sensor data $y(\boldsymbol{n})$, note that recovering either representation of $\boldsymbol{x}(\boldsymbol{n})$ is equivalent. Moreover, the representation of (3) allows us to re-cast the pure-color sampling structure of (2) in terms of sampling structures associated with the difference channels x_α and x_β.

3) Fourier Analysis of Pure-Color CFAS: It is known how to explicitly compute the Fourier representation induced by the spatial subsampling of certain CFA patterns; for the case of the Bayer pattern, see [2], [3], and [6]. Here, however, we provide for a Fourier representation of all rectangular, periodic, pure-color CFAs in terms of the sublattice $\Lambda_{\boldsymbol{M}}$ associated with a given 3-partition $(\boldsymbol{M}, \Psi_r, \Psi_b)$ of $\mathbb{Z}^2$. Owing to their Abelian structure, lattices admit the notion of a Fourier transform as specified by a dual or reciprocal lattice. The spectral periodicity properties of a color image sampled along a lattice $\Lambda_{\boldsymbol{M}}$ are determined by its dual lattice $\widehat{\Lambda}_{\boldsymbol{M}}$ (the Poisson summation formula being a simple univariate example), thereby enabling us to characterize the effect on individual color channels of the spatio-spectral sampling induced by various CFA patterns.

According to the discrete and periodic nature of repeating pure-color CFA sampling patterns, the dual lattice $\widehat{\Lambda}_{\boldsymbol{M}}$ defines a unit cell about the origin in $\mathbb{R}^2$ with associated volume $\mathrm{vol}(\widehat{\Lambda}_{\boldsymbol{M}}) = (2\pi)^2/\mathrm{vol}(\Lambda_{\boldsymbol{M}})$, copies of which in turn form a tessellation of the spatial frequency plane.[3] Under our normalization of the Fourier transform, the dual lattice $\widehat{\Lambda}_{\boldsymbol{M}} = 2\pi \boldsymbol{M}^{-T}\mathbb{Z}^2$ associated with an admissible sampling matrix $\boldsymbol{M}$ will in turn admit $2\pi\mathbb{Z} \times 2\pi\mathbb{Z}$ as a sublattice. As our model for sensor geometry is the lattice $\mathbb{Z}^2$, it thus suffices to restrict our attention to dual lattice points contained in the unit cell $[-\pi, \pi) \times [-\pi, \pi)$ in the spatial frequency plane, which comprise a set of coset representatives for the sublattice $2\pi\mathbb{Z} \times 2\pi\mathbb{Z}$ in $\widehat{\Lambda}_{\boldsymbol{M}}$ (see, e.g., [10]).

We are now equipped to provide the main result of this section: a characterization of the spatio-spectral properties of images acquired under pure-color CFAs. Let $\mathcal{F}x$ denote the 2-D Fourier transform operator applied to $x(\boldsymbol{n})$, with $X(\boldsymbol{\omega}) := \mathcal{F}x$ parameterized by angular frequency $\boldsymbol{\omega} \in \mathbb{R}^2$. Recalling our earlier pixel-wise definition of a pure-color CFA associated with 3-partition $(\boldsymbol{M}, \Psi_r, \Psi_b)$ according to (2), we see that CFA components $c_r(\boldsymbol{n})$ and $c_b(\boldsymbol{n})$ are obtained

$$c_r(\boldsymbol{n}) = \mathcal{F}^{-1}\left\{ \mathrm{vol}(\Lambda_{\boldsymbol{M}})^{-1} \sum_{\boldsymbol{\lambda} \in \{\widehat{\Lambda}_{\boldsymbol{M}} \cap [-\pi,\pi)^2\}} \sum_{\boldsymbol{\psi} \in \Psi_r} e^{-j\boldsymbol{\psi}^T\boldsymbol{\lambda}} \delta(\boldsymbol{\omega} - \boldsymbol{\lambda}) \right\}$$

$$c_b(\boldsymbol{n}) = \mathcal{F}^{-1}\left\{ \mathrm{vol}(\Lambda_{\boldsymbol{M}})^{-1} \sum_{\boldsymbol{\lambda} \in \{\widehat{\Lambda}_{\boldsymbol{M}} \cap [-\pi,\pi)^2\}} \sum_{\boldsymbol{\psi} \in \Psi_b} e^{-j\boldsymbol{\psi}^T\boldsymbol{\lambda}} \delta(\boldsymbol{\omega} - \boldsymbol{\lambda}) \right\}.$$

It then follows from (3) that the Fourier transform of sensor data $y(\boldsymbol{n})$ over dual lattice points contained in the unit cell $[-\pi, \pi) \times [-\pi, \pi)$ is given by

$$\begin{aligned} Y(\boldsymbol{\omega}) = X_g(\boldsymbol{\omega}) + \frac{1}{\mathrm{vol}(\Lambda_{\boldsymbol{M}})} \sum_{\boldsymbol{\lambda} \in \{\widehat{\Lambda}_{\boldsymbol{M}} \cap [-\pi,\pi)^2\}} \\ \cdot \left(\sum_{\boldsymbol{\psi} \in \Psi_r} e^{-j\boldsymbol{\psi}^T\boldsymbol{\lambda}} X_\alpha(\boldsymbol{\omega} - \boldsymbol{\lambda}) + \sum_{\boldsymbol{\psi} \in \Psi_b} e^{-j\boldsymbol{\psi}^T\boldsymbol{\lambda}} X_\beta(\boldsymbol{\omega} - \boldsymbol{\lambda}) \right). \end{aligned} \tag{4}$$

Thus, we see that the lattice structure of the chosen 3-partition induces spectral copies of the difference channels x_α and x_β centered about the set of carrier frequencies $\{\widehat{\Lambda}_{\boldsymbol{M}} \cap [-\pi, \pi)^2\}$. As restrictions of lattices, these sets will always include the origin—corresponding to "baseband" copies of the respective

[3] See [10] for a discussion of technical issues, such as defining the unit cell and Fourier transform with respect to unions of cosets as we do here.

difference channels. In this manner (4) may be interpreted as specifying a baseband "luminance" signal

$$X_\ell(\boldsymbol{\omega}) := X_g(\boldsymbol{\omega}) + \frac{|\Psi_r|}{\mathrm{vol}(\Lambda_{\boldsymbol{M}})} X_\alpha(\boldsymbol{\omega}) + \frac{|\Psi_b|}{\mathrm{vol}(\Lambda_{\boldsymbol{M}})} X_\beta(\boldsymbol{\omega})$$

with the remainder of its terms comprising lower-bandwidth "chrominance" information modulated away from the origin. Recalling the interpretation of $\mathrm{vol}(\Lambda_{\boldsymbol{M}})$ as the maximum number of distinct colors supported by a given CFA, we see that the ratios of color components comprising luminance information depend directly on $|\Psi_r|$ and $|\Psi_b|$, the number of coset vectors associated with difference channels x_α and x_β.

An example of the baseband signal $X_\ell(\boldsymbol{\omega})$ corresponding to a typical color image is shown in Fig. 3(e); the locations of spectral replicates modulated away from the origin are shown in Fig. 2 for several 3-partitions corresponding to pure-color CFA patterns in wide use. From these examples, it may be seen that aliasing occurs whenever there is pairwise overlap of the spectral supports of $X_g(\boldsymbol{\omega})$, $\{X_\alpha(\boldsymbol{\omega}-\boldsymbol{\lambda}) : \boldsymbol{\lambda} \neq 0\}$, and $\{X_\beta(\boldsymbol{\omega}-\boldsymbol{\lambda}) : \boldsymbol{\lambda} \neq 0\}$, for $\boldsymbol{\lambda} \in \{\widehat{\Lambda}_{\boldsymbol{M}} \cap [-\pi,\pi)^2\}$. In the absence of aliasing, chrominance information can be successfully "demodulated" and then used to recover $X_g(\boldsymbol{\omega})$ from the baseband luminance channel $X_\ell(\boldsymbol{\omega})$ via standard filtering techniques; however, for each instance depicted in Fig. 2, the placement of chrominance information in the spatial frequency plane is seen to result in aliasing.

Further inspection confirms that in fact each of these patterns is sub-optimal from an aliasing perspective—a notion we formalize in Section II-B below. We begin by making precise the minimal assumptions on color channel bandwidths necessary to formulate this argument rigorously:

Assumption 1 (Bounded Bandwidth): We assume the supports of (X_g, X_α, X_β) to be bounded, such that the associated luminance and chrominance channels comprising (4) are contained in balls of radii $r_\ell < \pi$ and $r_c < \pi$, respectively.

Assumption 2 (Total Bandwidth): We assume $r_\ell + r_c > \pi$. This implies that the physical resolution of our image sensor is such that aliasing may in fact occur, depending on the placement of chrominance information in the Fourier domain.

Assumption 3 (Relative Bandwidth): We assume $r_\ell > r_c$. This is consistent with empirically reported results in the literature, following the documented correlation of color channels.

These assumptions imply that in order to *maximize* the allowable spectral radii r_ℓ and r_c subject to the zero-aliasing constraint required for perfect reconstruction, spectral replicates representing chrominance information should be placed along the perimeter of the unit cell $[-\pi,\pi) \times [-\pi,\pi)$ in the spatial frequency plane. The CFA patterns of Fig. 2(d)–(f) and (i)–(k) may be seen by inspection to violate this condition. Moreover, it follows from Assumption 3 that the *least* optimal placement of spectral replicates along this perimeter is about the points $(-\pi, 0)$ and $(0, -\pi)$—as these points *minimize* the maximum allowable spectral radii. As may be seen in Fig. 2(a)–(c) and (g), (h), (j), (k), the popular Bayer pattern and many others are sub-optimal from this perspective. Moreover, by reducing allowable channel bandwidth along the coordinate axes, these patterns are sensitive to the very horizontal and vertical features which frequently dominate typical images [24].

B. Sub-Optimality of Pure-Color CFAs: Statement and Proof

From the arguments and assumptions above, we conclude that neither pure-color nor panchromatic CFA designs currently in use are optimal from the perspective of spatial aliasing. We will later introduce new panchromatic CFA designs that *are* optimal from this perspective, but first we show that no periodic, pure-color CFA design can ever attain optimality—a fact reflected by the failure in practice of simple linear reconstruction methods when used with such patterns.

In essence, these patterns determine a lattice that packs luminance and chrominance information into the unit cell $[-\pi,\pi) \times [-\pi,\pi)$. Intuition suggests—and the above spatio-spectral analysis confirms—that a sphere-*packing* strategy is required, rather than the sphere-*filling* approach of current patterns. Accordingly, we first exhibit the spatio-spectral requirements necessary to maximize the allowable spectral radii r_ℓ and r_c, subject to the constraint of zero aliasing. To this end, suppose that Assumptions 1–3 hold, and consider a proper sublattice $\Lambda_{\boldsymbol{M}} \subset \mathbb{Z}^2$ along with a set Ψ of associated coset vectors. We then have the following proposition:

Proposition 1 (Bandwidth Maximization): Amongst all sets $\{\Psi+\Lambda_{\boldsymbol{M}}\}$, those that maximize $r_\ell+r_c$ subject to the constraint of zero aliasing take the following form: for every $\boldsymbol{\lambda} \in \{\widehat{\Lambda}_{\boldsymbol{M}} \cap [-\pi,\pi)^2\} \setminus \{(0,0)\}$ such that $\sum_{\boldsymbol{\psi}\in\Psi} \exp(-j\boldsymbol{\psi}^T\boldsymbol{\lambda}) \neq 0$, we have that $\|\boldsymbol{\lambda}\|_\infty = \pi$ and $\boldsymbol{\lambda} \notin \{(-\pi,0),(0,-\pi)\}$.

Recall from (4) that dual lattice points $\boldsymbol{\lambda} \neq (0,0)$ associated with nonzero weights $\sum_{\boldsymbol{\psi}\in\Psi} \exp(-j\boldsymbol{\psi}^T\boldsymbol{\lambda})$ represent "carrier frequencies" for chrominance information. The proposition thus specifies that in order to simultaneously maximize the allowable bandwidth of luminance and chrominance, all such carrier frequencies contained in the Fourier-domain unit cell $[-\pi,\pi)^2$ must be placed maximally far from the origin.

Proof: Consider radii r_ℓ and r_c as rays in the Cartesian plane which define balls representing the respective maximal directional bandwidths of luminance and chrominance information, as per Assumption 1. A sole ball representing luminance is centered about the origin, and each chrominance ball is taken to be centered around a candidate lattice point $\boldsymbol{\lambda} \in [-\pi,\pi)^2 \setminus \{(0,0)\}$ for which $\sum_{\boldsymbol{\psi}\in\Psi} \exp(-j\boldsymbol{\psi}^T\boldsymbol{\lambda}) \neq 0$. We then seek the set of $\boldsymbol{\lambda}$ yielding an arrangement that admits, with no intersection of spheres, the maximal $|r_\ell| + |r_c|$.

Assumption 3 ($|r_\ell| > |r_c|$) in turn implies that we need only consider the case of chrominance-luminance aliasing, rather than chrominance-chrominance aliasing. Noting that $|r_\ell + r_c| \leq |r_\ell| + |r_c|$, with equality if and only if r_ℓ and r_c are collinear, we may, therefore, take r_ℓ to be a ray emanating from the origin, and r_c to be a collinear ray emanating from any other candidate point $\boldsymbol{\lambda}$. For any angle taken by rays r_ℓ and r_c, the maximum of $|r_\ell + r_c| = |r_\ell| + |r_c|$ is attained by $\{\boldsymbol{\lambda} \in [-\pi,\pi)^2 : \|\boldsymbol{\lambda}\|_\infty = \pi\}$. Amongst all members of this set, Assumption 2 ($|r_\ell| + |r_c| > \pi$) excludes the set of points $\{(-\pi,0),(0,-\pi)\}$, and the proposition is thereby proved. ■

The following proposition in turn provides an upper bound on the volume of any sublattice $\Lambda_{\boldsymbol{M}} \subset \mathbb{Z}^2$ satisfying the condition for bandwidth maximization specified by Proposition 1:

Proposition 2 (Volume Limitation): Let $(\boldsymbol{M}, \Psi)$ determine a sampling set $\{\Psi+\Lambda_{\boldsymbol{M}}\}$ taking the bandwidth-maximizing form of Proposition 1. Then $\mathrm{vol}(\Lambda_{\boldsymbol{M}}) \leq 2|\Psi|$.

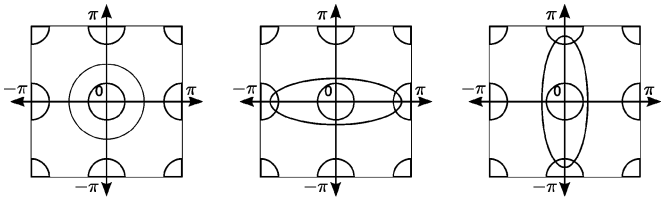

Fig. 4. Idealized spectral support of the channels (x_g, x_α, x_β) of a color image acquired under the Bayer pattern, showing alias-inducing replications.

The proof of this proposition is provided in Appendix I. Together, Propositions 1 and 2 imply the sub-optimality of periodic, pure-color CFA designs with respect to aliasing considerations. Indeed, it follows from these propositions that any such design that seeks to maximize the allowable spectral radii of luminance and chrominance cannot simultaneously admit three distinct colors. To see this, suppose that a 3-partition $(\boldsymbol{M}, \Psi_r, \Psi_b)$ is designed such that mutually exclusive sampling sets $\{\Psi_r + \Lambda_{\boldsymbol{M}}\}$ and $\{\Psi_b + \Lambda_{\boldsymbol{M}}\}$ both satisfy the conditions of Proposition 1. Then by Proposition 2 we have that $\mathrm{vol}(\Lambda_{\boldsymbol{M}}) \leq |\Psi_r| + |\Psi_b|$, but it follows from our earlier definition of a 3-partition that $\mathrm{vol}(\Lambda_{\boldsymbol{M}}) = |\Psi_r| + |\Psi_g| + |\Psi_b|$. We, therefore, conclude that the set of coset vectors Ψ_g indexing the sampling of our third color component must be empty.

C. Aliased Sensor Data and Demosaicking

The preceding discussion confirms the sub-optimality of all periodic, pure-color CFA patterns with respect to the metric of spatial aliasing. However, owing to the prevalence of the Bayer pattern in currently manufactured still and video digital cameras, much attention has been given to the problem of demosaicking color images acquired in this manner [4], [23], [25]–[34]. An ideal demosaicking solution would exhibit two main traits: low computational complexity for efficient hardware implementation, and amenability to analysis for accurate color fidelity and noise suppression. For instance, in the absence of further assumptions on the relationships amongst tristimulus values, the optimal *linear* reconstruction is indicated by an orthogonal projection onto the space of bandlimited functions, applied separately to each subsampled color channel. However, it is well known that this solution produces unacceptable artifacts, as aliasing prevents perfect reconstruction (see Fig. 4). Indeed, recalling Figs. 1 and 2, this follows precisely from the sub-optimality of pure-color CFAs with respect to aliasing.

As such, most demosaicking algorithms described in the literature make use (either implicitly or explicitly) of correlation structure in the spatial frequency domain, often in the form of local sparsity or directional filtering [3], [25], [26], [32], [35]. As noted in our earlier discussion, the set of carrier frequencies induced by the Bayer pattern includes $(-\pi, 0)$ and $(0, -\pi)$, locations that are particularly susceptible to aliasing by horizontal and vertical edges. Fig. 4(b) and (c) indicates these scenarios, respectively; it may be seen that in contrast to the radially symmetric baseband spectrum of Fig. 4(a), chrominance-luminance aliasing occurs along one of either the horizontal or vertical axes. However, successful reconstruction can still occur if a noncorrupted copy of this chrominance information is recovered, thereby explaining the popularity of (nonlinear) directional filtering steps [3], [32], [35]. We can, therefore, view the CFA design problem as one of spatial-frequency multiplexing, and the CFA demosaicking problem as one of demultiplexing to recover subcarriers, with spectral aliasing given the interpretation of "cross talk" [3].

On the basis of the above discussion, it is fair to conclude that existing linear interpolation schemes often lead to undesirable (and commercially unacceptable) distortion and visual artifacts. However, more sophisticated schemes are typically highly nonlinear and can be costly to implement in typical ASIC and DSP hardware environments. Moreover, nonlinear techniques, such as those requiring local edge detection, further exacerbate the problem of characterizing (and, hence, mitigating) the various sources of noise associated with the image acquisition process. Robustness of the detection variable, sensitivity to noise, and overall model accuracy all affect the quality of reconstruction. To this end, recent work has demonstrated the inadequacies of treating the denoising and interpolation tasks separately—a fact well known in industry—and has led to a number of methods designed to treat these problems jointly [6], [33], [34], [36].

III. Design: Alternative Patterns and Algorithms

Owing to the sub-optimality of periodic, pure-color CFA designs as proved in Section II-B above, the *optimal* periodic designs of CFA patterns are necessarily panchromatic. In this section, we pursue this design task by considering the *spectral* wavelength sampling requirements as well as the *spatial* sampling requirements associated with the image acquisition process. Assuming a regular, repeating rectangular pattern, and putting aside issues of white-balancing and sensor noise, the analysis above motivates us to consider *linear combinations* of prototype pure-color filters,[4] rather than restricting the values $c_r(\boldsymbol{n}), c_g(\boldsymbol{n}), c_b(\boldsymbol{n})$ to the set $\{0, 1\}$ implied by pure-color designs. Hence, we let $0 \leq c_r(\boldsymbol{n}), c_g(\boldsymbol{n}), c_b(\boldsymbol{n}) \leq 1$ indicate the array, with each value now representing a *mixture* of colors.

Though panchromaticity implies that the notion of a 3-partition $(\boldsymbol{M}, \Psi_r, \Psi_b)$ and its associated lattice structure no longer applies, we will instead use the Fourier-domain principles introduced in Section II to directly specify the chrominance carrier frequencies $\boldsymbol{\lambda}_i$ of interest. In this manner we may fulfill the optimality condition of Proposition 1, whereupon the risk of aliasing is reduced and, hence, overall image integrity is better preserved by the sensor data. As we show, image data acquired in this manner are easily manipulated, enjoy simple reconstruction schemes, and admit favorable computation-quality trade-offs with respect to subsequent processing in the imaging pipeline.

A. Optimal Panchromatic CFA Design Methodology

We now outline a method of spatio-spectral CFA design that satisfies the bandwidth maximization property of Proposition 1. First, define $c_\alpha(\boldsymbol{n}) := (c_r(\boldsymbol{n}) - \mu_\alpha)/\rho$, and $c_\beta(\boldsymbol{n}) := (c_b(\boldsymbol{n}) - \mu_\beta)/\rho$, where μ_α and μ_β are the DC components of c_r and c_b,

[4]Recent work has also focused on optimizing the spectral sensitivity functions of these prototype filters directly [8].

respectively, and ρ and γ are constants whose role as design parameters will become clear shortly. If we impose the convexity constraint $c_r + c_g + c_b = \gamma$, then (3) becomes

$$y(\boldsymbol{n}) = \begin{bmatrix} c_r(\boldsymbol{n}) & \gamma & c_b(\boldsymbol{n}) \end{bmatrix} \begin{bmatrix} x_\alpha(\boldsymbol{n}) \\ x_g(\boldsymbol{n}) \\ x_\beta(\boldsymbol{n}) \end{bmatrix}$$
$$= \begin{bmatrix} c_r(\boldsymbol{n}) \\ \gamma \\ c_b(\boldsymbol{n}) \end{bmatrix}^T \begin{bmatrix} 1 & 0 & 0 \\ \frac{-\mu_\alpha}{\gamma} & 1 & \frac{-\mu_\beta}{\gamma} \\ 0 & 0 & 1 \end{bmatrix} \begin{bmatrix} 1 & 0 & 0 \\ \frac{\mu_\alpha}{\gamma} & 1 & \frac{\mu_\beta}{\gamma} \\ 0 & 0 & 1 \end{bmatrix}$$
$$\times \begin{bmatrix} x_\alpha(\boldsymbol{n}) \\ x_g(\boldsymbol{n}) \\ x_\beta(\boldsymbol{n}) \end{bmatrix} = \begin{bmatrix} \rho c_\alpha(\boldsymbol{n}) & \gamma & \rho c_\beta(\boldsymbol{n}) \end{bmatrix} \begin{bmatrix} x_\alpha(\boldsymbol{n}) \\ x_\ell(\boldsymbol{n}) \\ x_\beta(\boldsymbol{n}) \end{bmatrix}$$

where $x_\ell(\boldsymbol{n}) = x_g(\boldsymbol{n}) + (\mu_\alpha/\gamma)x_\alpha(\boldsymbol{n}) + (\mu_\beta/\gamma)x_\beta(\boldsymbol{n})$ is now the baseband signal that can be taken to represent luminance.

Recalling the lowpass properties of $x_\alpha(\boldsymbol{n})$ and $x_\beta(\boldsymbol{n})$, our formulation of the CFA design problem enables us to *modulate* these terms via multiplication with $c_\alpha(\boldsymbol{n})$ and $c_\beta(\boldsymbol{n})$ such that the Fourier transforms of the frequency-modulated difference images are *maximally separated* from the baseband spectrum $X_\ell = \mathcal{F}x_\ell$. To accomplish this task, let us assume that the Fourier transforms of c_α and c_β, respectively, take the form

$$\begin{cases} C_\alpha(\boldsymbol{\omega}) = \sum_i \left[s_i \delta(\boldsymbol{\omega} + \boldsymbol{\lambda}_i) + \bar{s}_i \delta(\boldsymbol{\omega} - \boldsymbol{\lambda}_i) \right] \\ C_\beta(\boldsymbol{\omega}) = \sum_i \left[t_i \delta(\boldsymbol{\omega} + \boldsymbol{\lambda}_i) + \bar{t}_i \delta(\boldsymbol{\omega} - \boldsymbol{\lambda}_i) \right] \end{cases} \tag{5}$$

where $\bar{\cdot}$ denotes complex conjugation, $\boldsymbol{\lambda}_i \in \mathbb{R}^2$ the carrier frequencies, and $s_i, t_i \in \mathbb{C}$ the corresponding weights (with conjugate symmetry ensuring that the resultant c_α and c_β are real-valued). It follows that the sensor observations y are the sum of X_ℓ and the modulated versions of X_α and X_β

$$Y(\boldsymbol{\omega}) = \gamma X_\ell(\boldsymbol{\omega}) + \rho \sum_i \Big[(s_i X_\alpha + t_i X_\beta)(\boldsymbol{\omega} + \boldsymbol{\lambda}_i) + (\bar{s}_i X_\alpha + \bar{t}_i X_\beta)(\boldsymbol{\omega} - \boldsymbol{\lambda}_i) \Big]. \tag{6}$$

This approach enables the specification of CFA design parameters directly in the Fourier domain, by way of carrier frequencies $\{\boldsymbol{\lambda}_i\}$ and weights $\{s_i, t_i\}$. In keeping with Proposition 1, we enforce the restriction $\|\boldsymbol{\lambda}_i\|_\infty = \pi$ and $\boldsymbol{\lambda}_i \notin \{(-\pi, 0), (0, -\pi)\}$. Determination of the resultant color filters as a function of parameters $\mu_\alpha, \mu_\beta, \rho, \gamma$ then follows from inverse Fourier transforms $c_\alpha = \mathcal{F}^{-1}C_\alpha$ and $c_\beta = \mathcal{F}^{-1}C_\beta$

$$\begin{aligned} c_r(\boldsymbol{n}) &= \rho c_\alpha(\boldsymbol{n}) + \mu_\alpha \\ c_b(\boldsymbol{n}) &= \rho c_\beta(\boldsymbol{n}) + \mu_\beta \\ c_g(\boldsymbol{n}) &= \gamma - c_r(\boldsymbol{n}) - c_b(\boldsymbol{n}). \end{aligned}$$

Recall that in order to ensure physical realizability of the resultant CFA, we must have $0 \leq c_r(\boldsymbol{n}), c_g(\boldsymbol{n}), c_b(\boldsymbol{n}) \leq 1$. To accomplish this, first define $\nu_\alpha := \min_{\boldsymbol{n}} c_\alpha(\boldsymbol{n})$, $\nu_\beta := \min_{\boldsymbol{n}} c_\beta(\boldsymbol{n})$, and $\kappa := \max_{\boldsymbol{n}}(c_\alpha(\boldsymbol{n}) + c_\beta(\boldsymbol{n}))$. If we assign

$$\rho^{-1} = \max_{\boldsymbol{n}} \left(c_\alpha(\boldsymbol{n}) - \nu_\alpha, c_\beta(\boldsymbol{n}) - \nu_\beta, \kappa - c_\alpha(\boldsymbol{n}) - c_\beta(\boldsymbol{n}) \right)$$
$$\mu_\alpha = -\rho\nu_\alpha, \quad \mu_\beta = -\rho\nu_\beta, \quad \gamma = \rho(\kappa - \nu_\alpha - \nu_\beta)$$

it follows that our resultant CFA design may be expressed as

$$\begin{aligned} c_r(\boldsymbol{n}) &= \rho(c_\alpha(\boldsymbol{n}) - \nu_\alpha) \\ c_b(\boldsymbol{n}) &= \rho(c_\beta(\boldsymbol{n}) - \nu_\beta) \\ c_g(\boldsymbol{n}) &= \rho(\kappa - c_\alpha(\boldsymbol{n}) - c_\beta(\boldsymbol{n})). \end{aligned} \tag{7}$$

Here, the offsets μ_α and μ_β ensure nonnegativity of c_r and c_b, because $\rho c_\alpha \geq -\mu_\alpha$ and $\rho c_\beta \geq -\mu_\beta$. The constant γ guarantees nonnegativity of c_g, because $c_g = \gamma - c_r - c_b$ and $\rho\kappa \geq \rho(c_\alpha + c_\beta)$. Finally, the maximum value of $c_r(\boldsymbol{n})$, $c_g(\boldsymbol{n})$, $c_b(\boldsymbol{n})$ is equal to 1, owing to the multiplier ρ.

B. Features of the Optimal Panchromatic Designs

An important feature of the framework outlined above is that carrier frequencies $\{\boldsymbol{\lambda}_i\}$ and their weights $\{s_i, t_i\}$ are specified directly, with (5) and (7) ensuring that the resultant CFA is physically realizable. Patterns designed in this manner are panchromatic by definition, as they satisfy the conditions of Proposition 1 yet support three color components; however, recalling the discussion following Assumptions 1–3, they avoid the shortcomings of previously proposed panchromatic CFA designs. The convexity constraint $\gamma = c_r + c_g + c_b$ helps to ensure uniform quantum efficiency of the pixel sensors across the image plane, an important consideration to avoid under- and over-saturated sensor measurements within a single image. Moreover, CFAs are often implemented as a combination of so-called "subtractive" colors in practice—implemented as a stack of one or more inorganic films configured to attenuate the transmittance via the absorption of photons at specified wavelengths—in which case the condition $\max_{\boldsymbol{n}}(c_r(\boldsymbol{n}), c_g(\boldsymbol{n}), c_b(\boldsymbol{n})) = 1$ ensures that as many photons as possible will penetrate the physical filters.

While our design method does not explicitly take into account the effects of different illuminants, we note that it is predicated solely on Assumption 3, which states that the bandwidth of luminance exceeds that of chrominance. Robustness of the resultant patterns to changes in illuminant, therefore, hinges on how well this relative bandwidth assumption holds under various lighting conditions. Noting that it is already incorporated into state-of-the-art Bayer demosaicking methods, we expect that designs generated by our approach will be no more sensitive to varying illuminants than existing schemes. If Assumption 3 is violated—causing an increase in aliasing due to the larger spectral support of chrominance information—it is still the case that spectral replicates induced by our panchromatic designs will be farther from the baseband luminance channel, thereby reducing the risk of chrominance-luminance aliasing effects for the sake of chrominance-chrominance ones. To conclude this section, we note that the specification of CFA patterns satisfying the requirements of Proposition 1 is not unique, as the problem of choosing the parameters $\{\boldsymbol{\lambda}_i, s_i, t_i\}$ in (5) is under-constrained. Based on (7), a parameter search may be conducted to determine panchromatic patterns that possess other desirable characteristics:

1) Periodicity of the CFA Pattern: Constraining components of $\boldsymbol{\lambda}_i$ to be rational multiples of π ensures periodicity of the resultant CFA. For example, letting components of $\boldsymbol{\lambda}_i$ be equal to multiples of $\pi/2$ induces a 4×4 pattern.

2) Numerical Stability of CFA Design: Owing to the modulation weights $\{s_i, t_i\}$, the observed sensor data at frequency $\boldsymbol{\lambda}_i$ corresponds to a mixture of difference channels x_α and x_β. Large singular values for this linear combination ensure their separability via a requisite matrix inversion, while "equal treatment" of x_α and x_β is made explicit by setting $|s_i| = |t_i|$.

3) Resilience to Illuminant Spectrum: The mixture of color components that appears in the baseband luminance signal x_ℓ is fixed for any given CFA pattern. Implicitly, therefore, patterns such as Bayer assume a change in illuminant to be a perturbation from the $1:2:1$ proportion of red, green, and blue. Following this logic, this baseband luminance can be adjusted to yield a mixture complementing the "average" illuminant color, in order to minimize deviation from it.

4) Pixel Sensor Quantum Efficiency: As noted above, γ is a proxy for the quantum efficiency of the pixel sensors. As a result, CFA designs with large γ and $\rho|s_i + t_i|$ values tolerate more noise, and, hence, are favorable for low-light sensing.

5) Amenability to Linear Reconstruction: A linear reconstruction method based on demodulation (see Section IV-C) is sensitive to image features oriented orthogonally to carrier frequency vectors $\boldsymbol{\lambda}_i$ (though this sensitivity is reduced relative to pure-color CFA sampling, due to the increased separation of luminance and chrominance information). Decreasing the total number of carriers, and placing them as far from the origin as possible, subject to the avoidance of chrominance-chrominance aliasing, may serve to further mitigate aliasing.

6) Demosaicking Performance: Lastly, using a diverse set of test images and demosaicking methods, color image acquisition and reconstruction can be simulated. A numerical evaluation of the resultant error yields an empirical measure of reconstructability that may be used to refine the CFA design.

C. Optimal Linear Reconstruction Methodology

We now describe a completely linear reconstruction methodology to accompany our new panchromatic CFA patterns, in which the sensor data are subjected to bandpass filtering in order to recover modulated chrominance information and effect a full-color reconstruction. Before proceeding, we caution the reader that the choice of reconstruction method greatly influences the quality of the output image. We do not claim to present recovery methods that are optimal overall; instead, we seek CFA designs that maximize recoverability by mitigating aliasing effects. To this end, we present the optimal *linear* reconstruction method as a reference, in order to compare sensitivity and robustness of various existing and new CFA patterns. The design and optimization of *nonlinear* demosaicking methods, which have the potential to further improve output image quality, are left as topics for future work.

Suppose that conjugate modulation sequences $\bar{c}_\alpha(\boldsymbol{n}) := c_\alpha(\boldsymbol{n})^{-1}$ and $\bar{c}_\beta(\boldsymbol{n}) := c_\beta(\boldsymbol{n})^{-1}$ exist.[5] When these sequences are orthogonal, the chrominance information can be recovered via a multiplication by the corresponding conjugate carrier frequency followed by lowpass filtering. Assuming no overlap amongst the supports of $X_\ell(\boldsymbol{\omega})$, $X_\alpha(\boldsymbol{\omega})$, and $X_\beta(\boldsymbol{\omega})$, we obtain exact reconstruction of the full-color image $\hat{\boldsymbol{x}}(\boldsymbol{n})$ as

$$\begin{bmatrix} \hat{x}_r(\boldsymbol{n}) \\ \hat{x}_g(\boldsymbol{n}) \\ \hat{x}_b(\boldsymbol{n}) \end{bmatrix} = \begin{bmatrix} 1 & 1 & 0 \\ 0 & 1 & 0 \\ 0 & 1 & 1 \end{bmatrix} \begin{bmatrix} \frac{1}{\rho} & 0 & 0 \\ \frac{-\mu_\alpha}{\gamma\rho} & \frac{1}{\gamma} & \frac{-\mu_\beta}{\gamma\rho} \\ 0 & 0 & \frac{1}{\rho} \end{bmatrix} \begin{bmatrix} h_\alpha * \bar{c}_\alpha y \\ h_\ell * y \\ h_\beta * \bar{c}_\beta y \end{bmatrix} \tag{8}$$

where $*$ denotes the discrete convolution operator, and the passbands of the lowpass filters $h_\alpha, h_\ell, h_\beta$ are assumed to match the respective bandwidths of the signals $x_\alpha, x_\ell, x_\beta$.

Given sufficient separation of the chrominance information in the frequency domain, even simple lowpass filters designed for efficiency will suffice for the reconstruction task. For example, a separable 2-D odd-length triangle filter—a linear-phase filter with modest frequency roll-off—can be easily implemented in existing ASIC or DSP architectures [37].

IV. Evaluation: Implementation and Experiments

We now provide instantiations of several new CFA patterns constructed using the design strategy proposed in Section III-A above, and demonstrate their superior performance in terms of aliasing minimization and mean-square reconstruction error.

A. Examples of Optimal Panchromatic CFA Patterns

We first show example $N \times N$ CFA patterns generated by conducting an exhaustive search for the optimal $\{\boldsymbol{\lambda}_i, s_i, t_i\}$ over a parameter space restricted to satisfy the following rules.

- $\|\boldsymbol{\lambda}_i\|_\infty = \pi$ and $\boldsymbol{\lambda}_i \notin \{(-\pi, 0), (0, -\pi)\}$ (Proposition 1).
- $\boldsymbol{\lambda}_i \in 2\pi\mathbb{Z}^2/N$ (induces $N \times N$ periodicity).
- Number of distinct carrier frequencies is limited to two.
- Red-green-blue ratio in x_ℓ is $1:1:1$ or $1:2:1$.

Amongst the set of parameters satisfying the above constraints, we then selected the combination yielding the largest singular values for the choice of weights $\{s_i, t_i\}$ (see Section III-B).

We report the resultant optimal parameters in Table I for $N = 4,6,8$; the corresponding patterns are shown in Fig. 5. Each of these new patterns is panchromatic, and may be asymmetric in the horizontal and vertical directions; all use fewer than $N \times N$ color filters in practice. Moreover, there are equal numbers of "neighboring" colors for each color used in the CFA pattern—a feature that simplifies the characterization of *cross-talk* noise (photon and electron leakages) [20]. Note also that the optimal 4×4 and 8×8 CFA patterns are identical.

B. Reduction of Aliasing Effects Using New CFA Patterns

To investigate the potential of these example patterns to reduce aliasing effects, two sets of test images were used to provide full-color proxy data: a standard set of twenty Kodak images originally acquired on film [4], and a set of six images measured at multiple wavelengths [38]. In keeping with standard practice, simulated data $\boldsymbol{y}(\boldsymbol{n})$ were obtained for each CFA pattern by "sensing" these images according to (3).

[5] We do not discuss cases in which there are zeros; however, our results are easily generalizable to such cases via an appropriate multiplicative constant.

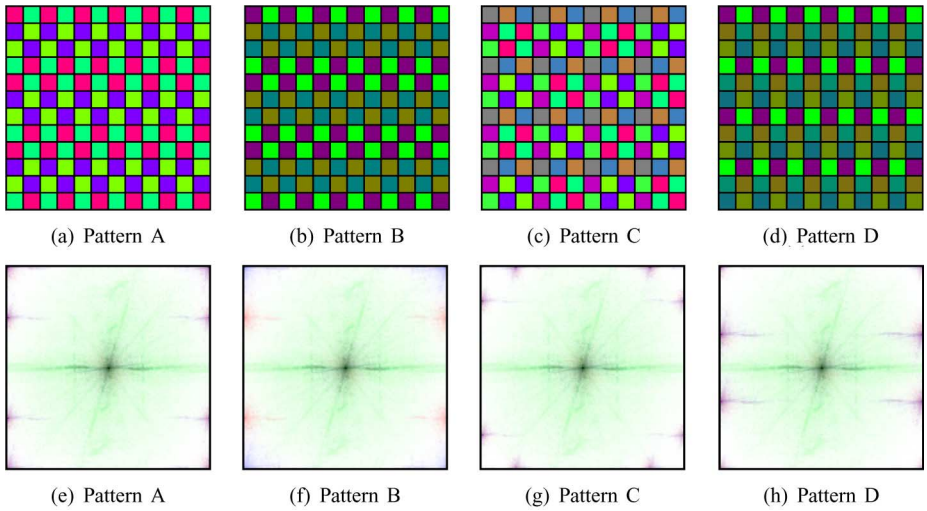

(a) Pattern A (b) Pattern B (c) Pattern C (d) Pattern D

(e) Pattern A (f) Pattern B (g) Pattern C (h) Pattern D

Fig. 5. Example CFA patterns generated using the parameters in Table I (top row), and corresponding "lighthouse" log-magnitude spectra (bottom row).

TABLE I
EXAMPLES OF PANCHROMATIC CFA PATTERNS SPECIFIED IN TERMS OF $\{\boldsymbol{\lambda}_i, s_i, t_i\}$

Pattern	$\{\boldsymbol{\lambda}_i, s_i, t_i\}$	$i=0$	$i=1$	N	R : G : B
A	$\boldsymbol{\lambda}_i$	$(\pi, \frac{\pi}{2})$	(π, π)	4×4, 8×8	1 : 1 : 1
	red s_i	$1+1i$	1		
	blue t_i	$1+1i$	-1		
B	$\boldsymbol{\lambda}_i$	$(\pi, \frac{\pi}{2})$	(π, π)	4×4, 8×8	1 : 2 : 1
	red s_i	$1+1i$	0		
	blue t_i	0	1		
C	$\boldsymbol{\lambda}_i$	$(\pi, \frac{2\pi}{3})$	$(\frac{2\pi}{3}, \pi)$	6×6	1 : 1 : 1
	red s_i	$1i$	$1i$		
	blue t_i	$1i$	$-1i$		
D	$\boldsymbol{\lambda}_i$	$(\pi, \frac{1\pi}{3})$	(π, π)	6×6	1 : 2 : 1
	red s_i	$3+4i$	1		
	blue t_i	$3-4i$	1		

We pause here to describe in more detail our image test sets, in particular the latter set of images measured at multiple wavelengths [38]. While the standard test set of Kodak images provide a widely accepted means of comparing various algorithms [4], we caution that numerical simulations using this test set are subject to uncertainties about how the digital image data were acquired (e.g., resolution, illumination) and whether they have undergone any additional processing (e.g., white-balancing, gamma correction). As a means of reducing these uncertainties to yield better-controlled experiments, we adopted directly measured multiwavelength image data [38] as an additional form of full-color proxy. In this case, we took the quantum efficiencies of our pure-color CFA values directly from the data sheet of a popular Sony sensor [39]; those of our proposed panchromatic designs are assumed to be linear combinations of these prototype pure-color responses.

To test the reduction in aliasing effects yielded by our new CFA designs, first recall from (4) and (6) that sensor data $Y(\boldsymbol{\omega})$ can be interpreted as a superposition of baseband luminance channel X_ℓ and chrominance information in the form of frequency-shifted versions of X_α and X_β. The mean-square error of a linear filter h_ℓ acting on y to estimate x_ℓ has the form $\sum_{\boldsymbol{n}} ||h_\ell(\boldsymbol{n}) * y(\boldsymbol{n}) - x_\ell(\boldsymbol{n})||^2$. Barring additional assumptions, the optimal filter in this case is given by Wiener–Hopf, whose expected squared error is shown in Appendix II for the case of mutually independent $\{x_\alpha, x_\ell, x_\beta\}$ to follow from (7) as

$$J_{x_\ell} := \int_{[-\pi,\pi)^2} \frac{\rho^2 S_{x_\ell}(\boldsymbol{\omega}) S_{x_\alpha, x_\beta}(\boldsymbol{\omega})}{S_y(\boldsymbol{\omega})} d\boldsymbol{\omega} \tag{9}$$

where S denotes a (cross-) power spectral density. Here, the quantity $S_{x_\ell}(\boldsymbol{\omega}) S_{x_\alpha, x_\beta}(\boldsymbol{\omega})$ corresponds to the inner product between the expected squared magnitudes of X_ℓ and the modulated versions of X_α and X_β; it evaluates to zero in the absence of aliasing, but is large when aliasing is severe. Thus, the integrand in (9) can be taken as a measure of aliasing relative to the magnitude of the sensor data, and is useful for comparing the performance of different CFA patterns.

In Table II, we report aliasing measurements J_{x_ℓ} for both sets of test images. In general, we see a significant decrease in aliasing severity when using proposed CFA designs A and C (patterns with a $1:1:1$ ratio of red-green-blue) rather than pure-color CFA patterns—a trend which is consistent across both sets of test images. We can also visualize the degree of aliasing associated with various CFAs by comparing the spectral content of the sensor data, as shown in Fig. 2 and the bottom row of Fig. 5. Owing to its higher modulation frequencies, the chrominance information illustrated in Fig. 5 is disjoint from the baseband luminance information. This reduces the *overall* risk of aliasing, relative to existing patterns—though any particular aliasing effects will depend on image content. For example, when presented with strong vertical image features, Pattern D is at a lower risk of aliasing than the Bayer pattern, but at a higher risk than Patterns A-C.

C. Improved Linear Reconstruction Using New CFA Patterns

To evaluate the potential of Patterns A–D for improved demosaicking performance, we employed three contemporary nonlinear demosaicking algorithms [4], [32], [40] to serve as a baseline in conjunction with the Bayer CFA pattern. We then employed the simple linear demosaicking scheme described in Section III-C for new panchromatic Patterns A–D, in which the sensor data $y(\boldsymbol{n})$ were subjected to bandpass filtering in order to reconstruct the full-color image $\hat{\boldsymbol{x}}(\boldsymbol{n})$ according to (8).

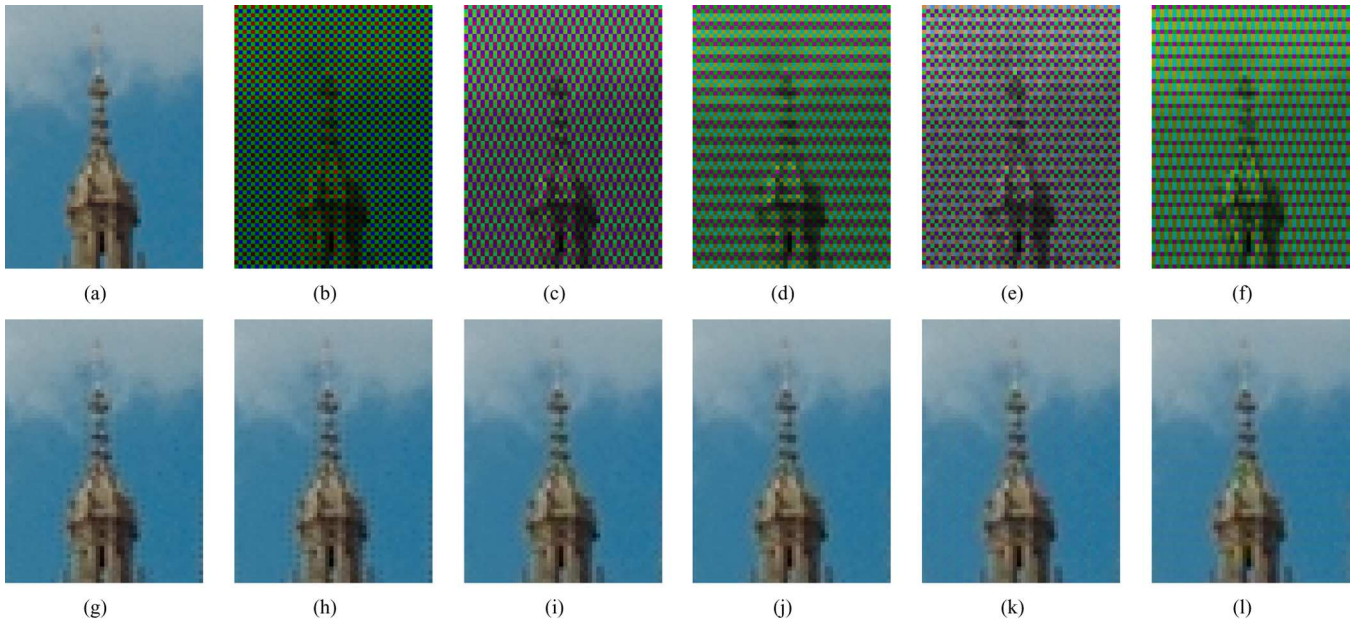

Fig. 6. Top row: (a) Detail of original "structure 11" image. (b-f) Sensor images using Bayer pattern, pattern A, pattern B, pattern C, and pattern D, respectively. Bottom row: (g) State-of-the-art nonlinear reconstruction of (b) according to [4]. (h-l) Optimal linear reconstruction of (b-f), respectively.

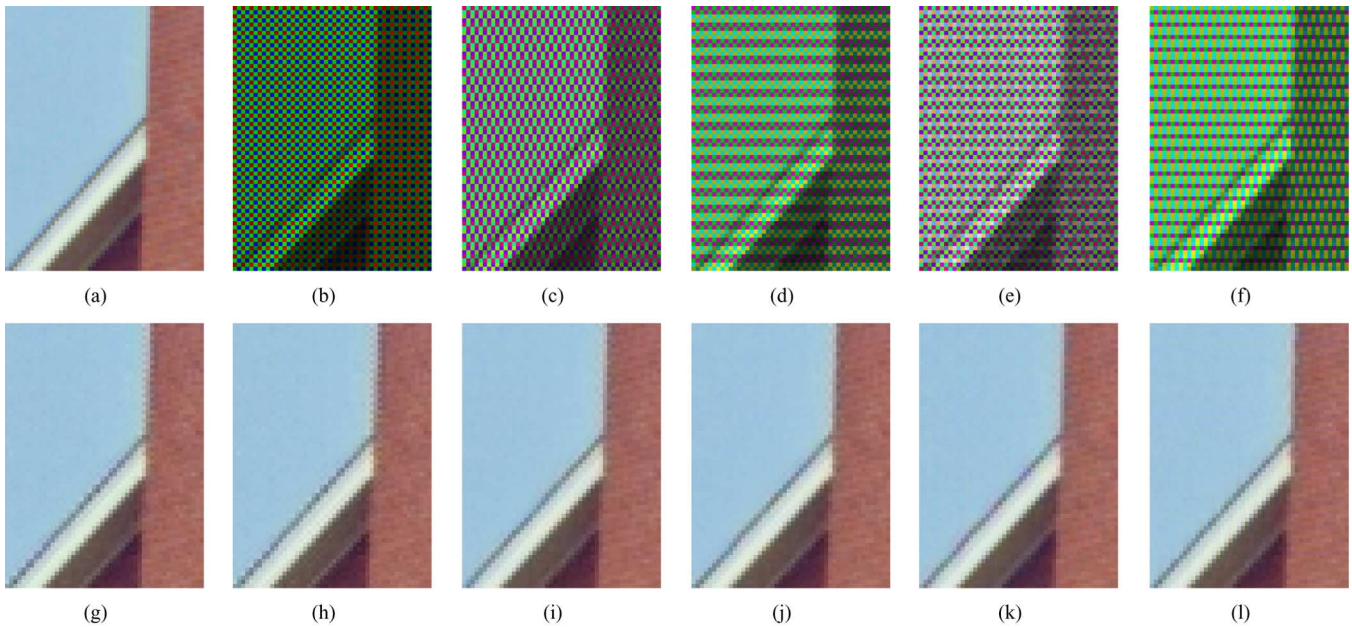

Fig. 7. Top row: (a) Detail of original "house" image. (b-f) Sensor images using Bayer pattern, pattern A, pattern B, pattern C, and pattern D, respectively. Bottom row: (g) State-of-the-art nonlinear reconstruction of (b) according to [4]. (h-l) Optimal linear reconstruction of (b-f), respectively.

To this end, Figs. 6–8(b)–(f) show simulated sensor data $y(\boldsymbol{n})$, acquired respectively via the Bayer pattern and proposed Patterns A-D, and represented here using an orthogonal projection of the full-color test images onto the subspace spanned by each respective color filter. By visual inspection, the contiguity of image features such as edges is better preserved in the proposed sensor images relative to the Bayer sensor image. For example, it is more difficult to discern object boundaries in Fig. 7(b) than in Fig. 7(c)–(f).

Though we again caution the reader that any color image reconstruction depends on the choice of algorithm as well as the choice of CFA pattern, demosaicking experiments provide some sense of the performance gains and trends that we may expect from the new class of spatio-spectral CFA designs introduced in this paper. To this end, Figs. 6–8(g)–(l) show examples of reconstructions corresponding to each sensor image. In comparison to the iterative, nonlinear demosaicking method of [4], we see that the reconstructions corresponding to our new panchromatic CFAs are significantly less prone to severe aliasing effects; they suffer much less from zippering artifacts yet preserve the sharpness of image features. Other noticeable differences are the less-jagged diagonal edges in Fig. 7(i)–(l), and the fact that certain textured regions, such as the ones in Fig. 8(i)–(l), do not suffer from artifacts.

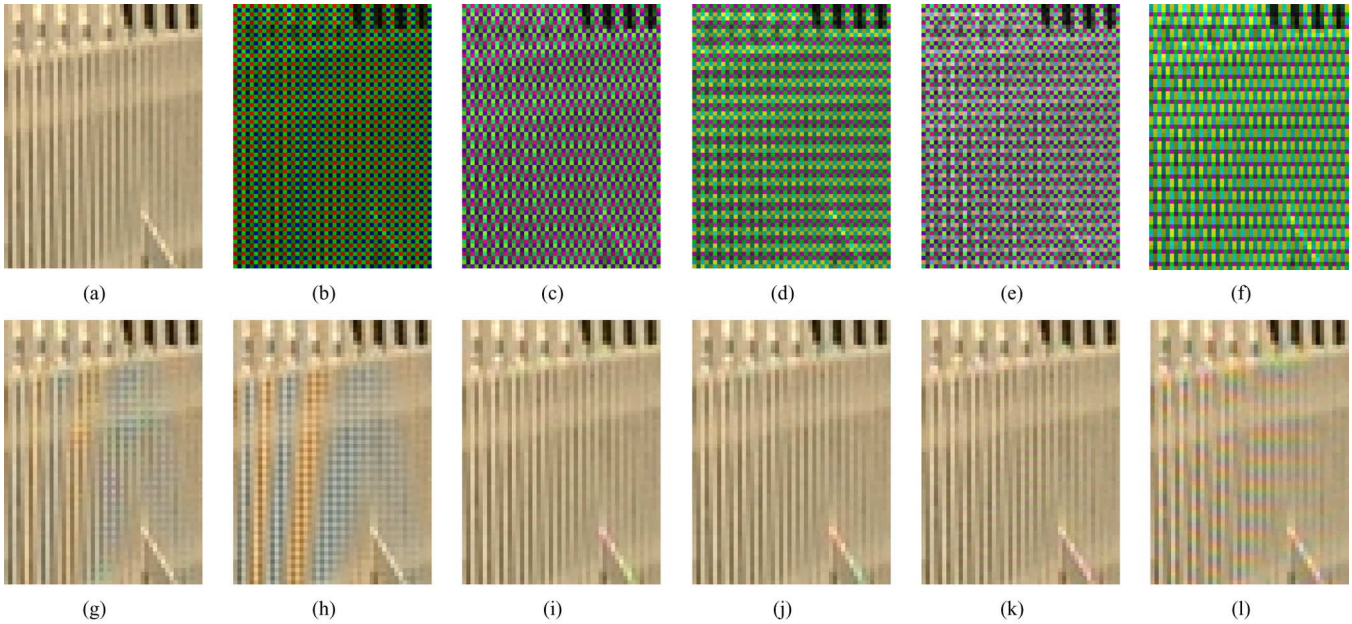

Fig. 8. Top row: (a) Detail of original "lighthouse" image. (b-f) Sensor images using Bayer pattern, pattern A, pattern B, pattern C, and pattern D, respectively. Bottom row: (g) State-of-the-art nonlinear reconstruction of (b) according to [4]. (h-l) Optimal linear reconstruction of (b-f), respectively.

These observations are reflected in the measurements of mean-square reconstruction error listed in Table III, whereupon it may be seen that entirely linear reconstructions under Patterns A and B consistently outperform even the state-of-the-art demosaicking algorithms applied to test data acquired under the Bayer pattern. Compared to a linear demosaicking of the Bayer sensor image for the same computational complexity, the proposed CFAs show significant and consistent improvements in both visual quality and mean-square reconstruction error. Overall, the differences for multiwavelength data are that the demosaicking algorithm of [32] now outperforms the methods in [4] and [40], and is comparable to the optimal linear reconstruction based on the color filter array of Pattern A.

As a final point, we note that the enhanced quantum efficiencies of the panchromatic color filters afforded by these new patterns appear to yield increased robustness to sensor noise—in addition to more tractable noise statistics (owing to linear demosaicking) that raise the possibility for postdemosaicking denoising. As an example, Fig. 9 shows reconstructions corresponding to those of Figs. 6–8, but for simulated sensor data subjected to Poisson noise, with no denoising applied. The corresponding noise contributions are seen by inspection to be less severe in reconstructions obtained from Pattern A than from the Bayer pattern, suggesting the potential for new reconstruction methods to lead to more accurate means of joint denoising and demosaicking [6].

V. Discussion

In this paper, we have proposed new panchromatic alternatives to existing CFA patterns, through a novel framework based on spatio-spectral sampling for color imaging. We posed the CFA design problem formally as one of simultaneously maximizing the spectral radii of luminance and chrominance channels subject to perfect reconstruction, and—after proving sub-optimality of a wide class of existing array patterns—provided a constructive method for its solution that yields robust new array designs implementable as subtractive colors. By specifying the desired spatio-spectral response directly in the Fourier domain and providing a corresponding set of optimization criteria, we were able to design patterns that increased the available spatial resolution for fixed sensor size.

This design methodology not only sheds light on the failure of simple, linear demosaicking methods in the case of existing color filter arrays such as the well-known Bayer pattern, but also provides for efficient linear demosaicking and a potential for improvements in reconstruction quality for natural images. Empirical evaluations on standard and multiwavelength color image test sets support our theoretical results, and indicate the potential of these patterns to increase spatial resolution for fixed sensor size, and to contribute to improved reconstruction fidelity as well as significantly reduced hardware complexity.

Appendix I
Proof of Proposition 2

Proof: Define $c(\boldsymbol{n}) = \sum_{\boldsymbol{n}_0 \in \{\Psi + \Lambda_{\boldsymbol{M}}\}} \delta(\boldsymbol{n} - \boldsymbol{n}_0) \in \{0, 1\}$, according to our definition of a pure-color CFA. The bandwidth maximization requirement set forth in Proposition 1 implies a unique Fourier reconstruction in $\boldsymbol{\omega} = (\omega_1, \omega_2)$ as

$$c(\boldsymbol{n}) = \mathcal{F}^{-1}\left\{ \mathrm{vol}(\Lambda_{\boldsymbol{M}})^{-1} \sum_{\boldsymbol{\lambda} \in \{\widehat{\Lambda}_{\boldsymbol{M}} \cap [-\pi, \pi)^2\}} \sum_{\boldsymbol{\psi} \in \Psi} e^{-j\boldsymbol{\psi}^T \boldsymbol{\lambda}} \delta(\boldsymbol{\omega} - \boldsymbol{\lambda}) \right\}$$

$$= \mathcal{F}^{-1}\left\{ \mathrm{vol}(\Lambda_{\boldsymbol{M}})^{-1} \sum_{\boldsymbol{\psi} \in \Psi} \sum_{\boldsymbol{\lambda} \in \{\widehat{\Lambda}_{\boldsymbol{M}} \cap \{\Omega_0 \cup \Omega_1 \cup \Omega_2 \cup \Omega_3\}\}} e^{-j\boldsymbol{\psi}^T \boldsymbol{\lambda}} \delta(\boldsymbol{\omega} - \boldsymbol{\lambda}) \right\}$$

where Proposition 1 implies that the allowable domain of $\boldsymbol{\lambda}$ in the spatial frequency plane is described by the following four

TABLE II
MEASURES OF CFA-DEPENDENT ALIASING IMPOSED ON X_ℓ BY X_α AND X_β

Image	Pure-Color CFA Patterns					Proposed CFA Patterns			
[23]; [38]	[11]	[12]	[20]	Vert.	Diag.	A	B	C	D
1	2183	2220	2177	2145	2124	943	2179	943	2177
2	986	981	983	1083	1080	480	984	480	983
3	1416	1413	1415	1408	1404	623	1414	624	1414
4	2482	2475	2479	2372	2372	1053	2478	1053	2476
5	1975	1969	1972	1951	1938	861	1973	862	1972
6	2905	2897	2899	2879	2867	1274	2900	1275	2900
7	2993	2980	2984	2924	2923	1299	2985	1299	2983
8	2628	2620	2623	2564	2564	1139	2625	1139	2624
9	1429	1424	1426	1419	1413	627	1427	627	1427
10	4192	4183	4186	4030	4028	1790	4190	1790	4188
11	1877	1798	1808	1716	1715	761	1800	762	1800
12	1621	1614	1615	1615	1614	717	1626	717	1615
13	1946	1971	1942	1895	1893	841	1944	841	1943
14	2123	2116	2118	2088	2087	927	2121	927	2119
15	1065	1067	1062	1068	1063	471	1064	471	1062
16	3211	3204	3205	3162	3161	1404	3210	1404	3208
17	6459	6455	6456	6350	6349	2821	6459	2822	6457
18	3090	3084	3086	3038	3022	1342	3087	1343	3086
19	1796	1789	1792	1801	1795	797	1791	797	1791
20	1808	1803	1805	1797	1787	794	1805	794	1804
Mean	2409	2403	2402	2365	2360	1048	2403	1048	2401
Median	2049	2043	2045	2020	2013	894	2047	894	2045
Minimum	986	981	983	1068	1063	471	984	471	983
Maximum	6459	6455	6456	6350	6349	2821	6459	2822	6457
Range	5474	5474	5473	5283	5287	2350	5476	2351	5475
Std. Dev.	1242	1241	1243	1206	1207	536	1243	536	1243
colorchecker	910	911	910	1032	1032	459	910	459	910
fruitandflowers	329	329	329	403	408	179	328	179	328
simage_hand	2342	2342	2342	2615	2613	1161	2342	1161	2342
woman_face	2703	2703	2707	2745	2747	1221	2704	1220	2705
woman_reading	3093	3093	3093	3209	3209	1426	3093	1426	3094
young_girl	2344	2344	2359	2380	2394	1056	2344	1056	2344
Mean	1954	1954	1957	2064	2067	917	1953	917	1954
Median	2343	2343	2350	2498	2503	1108	2343	1108	2343
Minimum	329	329	329	403	408	179	328	179	328
Maximum	3093	3093	3093	3209	3209	1426	3093	1426	3094
Range	2765	2765	2764	2806	2801	1247	2765	1247	2765
Std. Dev.	1086	1086	1087	1096	1095	487	1086	487	1086

mutually exclusive sets

$$\Omega_0 = 2\pi\mathbb{Z}^2$$
$$\Omega_1 = \{\boldsymbol{\lambda} : \boldsymbol{\lambda} \in \begin{bmatrix}\omega_1 \\ -\pi\end{bmatrix} + 2\pi\mathbb{Z}^2, \omega_1 \in (-\pi,\pi), \omega_1 \neq 0\}$$
$$\Omega_2 = \{\boldsymbol{\lambda} : \boldsymbol{\lambda} \in \begin{bmatrix}-\pi \\ \omega_2\end{bmatrix} + 2\pi\mathbb{Z}^2, \omega_2 \in (-\pi,\pi), \omega_2 \neq 0\}$$
$$\Omega_3 = \begin{bmatrix}-\pi \\ -\pi\end{bmatrix} + 2\pi\mathbb{Z}^2.$$

Because the set $\{\Omega_i \cap [-\pi,\pi)^2\}$ consists of either a point or two disjoint line segments for all i, the resultant inverse Fourier transform simplifies as follows:

$$\begin{aligned} c(\boldsymbol{n}) &= \sum_{i=0}^{3}\sum_{\boldsymbol{\psi}\in\Psi}\sum_{\boldsymbol{\lambda}\in\{\widehat{\Lambda}_{\boldsymbol{M}}\cap\Omega_i\cap[-\pi,\pi)^2\}} e^{j\boldsymbol{n}^T\boldsymbol{\lambda}}\frac{e^{-j\boldsymbol{\psi}^T\boldsymbol{\lambda}}}{\mathrm{vol}(\Lambda_{\boldsymbol{M}})} \\ &= e^{j0}\sum_{\boldsymbol{\psi}\in\Psi}\sum_{\boldsymbol{\lambda}=(0,0)}\frac{e^{-j\boldsymbol{\psi}^T\boldsymbol{\lambda}}}{\mathrm{vol}(\Lambda_{\boldsymbol{M}})} \\ &\quad + e^{j\pi n_2}\sum_{\boldsymbol{\psi}\in\Psi}\sum_{\lambda_1\in(-\pi,\pi),\lambda_1\neq 0(\lambda_1,\pi),\in\widehat{\Lambda}_{\boldsymbol{M}}}\frac{e^{j(n_1-\psi_1)\lambda_1 - j\psi_2\pi}}{\mathrm{vol}(\Lambda_{\boldsymbol{M}})} \\ &\quad + e^{j\pi n_1}\sum_{\boldsymbol{\psi}\in\Psi}\sum_{\lambda_2\in(-\pi,\pi),\lambda_2\neq 0(\pi,\lambda_2),\in\widehat{\Lambda}_{\boldsymbol{M}}}\frac{e^{j(n_2-\psi_2)\lambda_2 - j\psi_1\pi}}{\mathrm{vol}(\Lambda_{\boldsymbol{M}})} \\ &\quad + e^{j\pi(n_1+n_2)}\sum_{\boldsymbol{\psi}\in\Psi}\sum_{\boldsymbol{\lambda}=(\pi,\pi)}\frac{e^{-j\boldsymbol{\psi}^T\boldsymbol{\lambda}}}{\mathrm{vol}(\Lambda_{\boldsymbol{M}})} \\ &= f_0 + (-1)^{n_2}f_1(n_1) + (-1)^{n_1}f_2(n_2) + (-1)^{n_1+n_2}f_3 \end{aligned}$$

where f_i denotes $\sum_{\boldsymbol{\psi}}\cdot$ in each respective term.

We now enumerate all scenarios concerning $\{f_i\}_{i=0}^3$, and show that $\mathrm{vol}(\Lambda_{\boldsymbol{M}}) \leq 2|\Psi|$ in every possible case. First, suppose f_1 and f_2 to be nonzero functions. Then it is easy to verify, using $(0,0),(\pi,\pi) \notin \Omega_1 \cup \Omega_2$, that there exist indices $\boldsymbol{n}', \boldsymbol{n}'' \in \mathbb{Z}^2$ such that $f_1(2n_1') \neq f_1(2n_1'')$ and $f_2(2n_2') \neq f_2(2n_2'')$. If we let $c(\boldsymbol{n}') = 1$ without loss of generality, then

$$f_0+f_3+f_1(2n_1')+f_2(2n_2') \neq f_0+f_3+f_1(2n_1')+f_2(2n_2'') = 0$$
$$f_0+f_3+f_1(2n_1')+f_2(2n_2') \neq f_0+f_3+f_1(2n_1'')+f_2(2n_2') = 0$$
$$f_0+f_3+f_1(2n_1'')+f_2(2n_2') \neq f_0+f_3+f_1(2n_1'')+f_2(2n_2'') = 1.$$

Otherwise put, we have that

$$f_0 + f_3 + \begin{bmatrix}1&0&1&0\\1&0&0&1\\0&1&1&0\\0&1&0&1\end{bmatrix}\begin{bmatrix}f_1(2n_1')\\f_1(2n_1'')\\f_2(2n_2')\\f_2(2n_2'')\end{bmatrix} = \begin{bmatrix}1\\0\\0\\1\end{bmatrix} \tag{10}$$

$$\Rightarrow \quad \begin{bmatrix}1&0&1&0\\1&0&0&1\\0&1&1&0\\0&1&0&1\end{bmatrix}\begin{bmatrix}f_1(2n_1')\\f_1(2n_1'')\\f_2(2n_2')\\f_2(2n_2'')\end{bmatrix} = \begin{bmatrix}1-f_0-f_3\\-f_0-f_3\\-f_0-f_3\\1-f_0-f_3\end{bmatrix}.$$

TABLE III
MEAN-SQUARE RECONSTRUCTION ERROR FOR VARIOUS CFA PATTERNS

Image	Bayer Pattern				Proposed Patterns			
[23]; [38]	Linear	[4]	[32]	[40]	A	B	C	D
1	18.41	11.22	20.11	9.41	8.19	9.24	15.66	17.51
2	8.58	7.63	8.14	6.92	6.02	6.73	15.57	16.76
3	15.83	11.67	18.64	14.81	13.73	16.06	18.44	26.91
4	12.82	9.24	11.36	7.98	5.99	6.98	11.28	12.25
5	6.33	4.67	5.82	4.60	4.23	4.52	6.87	7.46
6	39.81	19.34	27.30	16.87	13.32	15.37	20.21	42.08
7	6.61	4.49	5.24	4.20	4.00	4.35	5.77	7.78
8	5.20	4.37	5.70	4.32	3.77	4.16	5.53	6.82
9	10.42	7.94	11.48	8.04	6.72	7.40	11.10	14.39
10	5.40	3.82	4.42	3.61	2.92	3.20	5.13	6.81
11	24.01	23.84	47.49	21.33	22.83	25.05	45.36	39.23
12	8.80	8.15	10.79	8.58	6.85	7.60	11.08	13.78
13	6.55	4.52	4.63	4.21	2.52	2.73	4.96	4.34
14	5.26	4.91	7.72	5.17	5.07	5.65	7.17	9.28
15	13.43	12.66	23.35	13.88	12.83	13.97	21.77	20.83
16	13.31	6.96	9.48	6.60	5.43	6.18	8.34	14.90
17	6.76	5.90	8.14	6.14	5.43	6.12	7.95	11.54
18	11.17	8.56	14.30	8.16	6.73	7.38	12.18	11.76
19	12.57	10.88	15.01	11.45	8.60	9.20	12.48	14.69
20	21.32	22.66	32.87	24.60	16.14	17.58	23.97	25.42
Mean	12.63	9.67	14.60	9.55	8.07	8.97	13.54	16.23
Median	10.79	8.04	11.08	8.01	6.37	7.18	11.19	14.08
Minimum	5.20	3.82	4.42	3.61	2.52	2.73	4.96	4.34
Maximum	39.81	23.84	47.49	24.60	22.83	25.05	45.36	42.08
Range	34.61	20.03	43.07	20.99	20.31	22.32	40.40	37.74
Std. Dev.	8.38	5.96	11.09	5.93	5.18	5.75	9.45	10.27
colorchecker	26.12	22.63	11.72	26.07	16.82	17.70	20.95	25.80
fruitandflowers	23.15	18.62	16.49	20.78	14.33	15.58	17.55	19.38
simage_hand	4.09	2.83	1.68	2.56	2.54	2.56	10.15	10.92
woman_face	21.60	18.54	15.16	18.91	13.72	15.28	19.31	20.19
woman_reading	15.75	13.44	12.05	12.84	10.57	11.12	16.52	15.91
young_girl	32.53	29.32	25.28	34.09	21.94	23.68	26.92	32.20
Mean	20.54	17.56	13.73	19.21	13.32	14.32	18.57	20.73
Median	22.38	18.58	13.61	19.85	14.03	15.43	18.43	19.78
Minimum	4.09	2.83	1.68	2.56	2.54	2.56	10.15	10.92
Maximum	32.53	29.32	25.28	34.09	21.94	23.68	26.92	32.20
Range	28.44	26.49	23.60	31.53	19.40	21.12	16.77	21.28
Std. Dev.	9.76	8.94	7.68	10.85	6.50	7.07	5.52	7.47

The 4×4 matrix in (10) is rank 3 and its column space is orthogonal to $(-1,1,1,-1)$. However, the inner product of $(-1,1,1,-1)$ and $(1,0,0,1) - f_0 - f_3$ is nonzero regardless of the values of f_0 and f_3

$$\begin{aligned}(-1,1,1,-1)&((1,0,0,1) - f_0 - f_3)^T \\ &= -2(1 - f_0 - f_3) + 2(-f_0 - f_3) = -2 \neq 0.\end{aligned}$$

We conclude that the equality in (10) cannot hold, and thus obtain a direct contradiction to the hypothesis that f_1 and f_2 are both nonzero functions.

We next consider all remaining scenarios. Suppose first that f_1 is a nonzero function and f_2 is zero (or equivalently f_2 nonzero and f_1 zero). Then

$$\begin{aligned}c(\boldsymbol{n}) &= f_0 + (-1)^{n_2} f_1(n_1) + (-1)^{n_1+n_2} f_3 \\ &= f_0 + (-1)^{n_2}(f_1(n_1) + (-1)^{n_1} f_3).\end{aligned}$$

Because $f_0+(f_1(n_1)+(-1)^{n_1} f_3) \neq f_0-(f_1(n_1)+(-1)^{n_1} f_3)$, we conclude that $c(\boldsymbol{n}) = 1 - c(n_1, n_2 + 1)$, or equivalently, $\mathrm{vol}(\Lambda_{\boldsymbol{M}}) = 2|\Psi|$. If instead, we have that f_1, f_2 are zero and f_3 nonzero, $(\boldsymbol{M}, \Psi)$ determines quincunx sampling, whereupon $\mathrm{vol}(\Lambda_{\boldsymbol{M}}) = 2|\Psi|$. Lastly, if f_1, f_2, f_3 are zero, then $\Lambda_{\boldsymbol{M}}$ is an integer lattice, and we have that $\mathrm{vol}(\Lambda_{\boldsymbol{M}}) = |\Psi|$. Hence, we see that in all possible cases, $\mathrm{vol}(\Lambda_{\boldsymbol{M}}) \leq 2|\Psi|$. ■

APPENDIX II
ALIASING MEASURES DERIVED FROM WIENER-HOPF

The Wiener–Hopf filter in the case at hand may be defined in the Fourier domain as $H_\ell(\boldsymbol{\omega}) = S_{x_\ell,y}(\boldsymbol{\omega})/S_y(\boldsymbol{\omega})$, where S_y is the power spectral density of y and $S_{x_\ell,y}$ is the cross-spectral density of x_ℓ and y. If $\{x_\alpha, x_\ell, x_\beta\}$ are in turn assumed mutually independent, it follows from (7) that

$$\begin{aligned}S_{x_\ell,y}(\boldsymbol{\omega}) &= \gamma S_{x_\ell}(\boldsymbol{\omega}), \\ S_y(\boldsymbol{\omega}) &= \gamma^2 S_{x_\ell}(\boldsymbol{\omega}) + \rho^2 S_{x_\alpha,x_\beta}(\boldsymbol{\omega}) \\ S_{x_\alpha,x_\beta}(\boldsymbol{\omega}) &= \sum_i \Big[\{|s_i|^2 S_{x_\alpha} + |t_i|^2 S_{x_\beta}\}(\boldsymbol{\omega} + \boldsymbol{\lambda}_i) \\ &\qquad + \{|s_i|^2 S_{x_\alpha} + |t_i|^2 S_{x_\beta}\}(\boldsymbol{\omega} - \boldsymbol{\lambda}_i) \Big].\end{aligned}$$

We may then compute the expected squared error as

$$\begin{aligned}J_{x_\ell} &= \int_{[-\pi,\pi)^2} \frac{S_{x_\ell}(\boldsymbol{\omega}) S_y(\boldsymbol{\omega}) - |S_{x_\ell,y}(j\boldsymbol{\omega})|^2}{S_y(\boldsymbol{\omega})} d\boldsymbol{\omega} \\ &= \int_{[-\pi,\pi)^2} \frac{\rho^2 S_{x_\ell}(\boldsymbol{\omega}) S_{x_\alpha,x_\beta}(\boldsymbol{\omega})}{S_y(\boldsymbol{\omega})} d\boldsymbol{\omega}.\end{aligned}$$

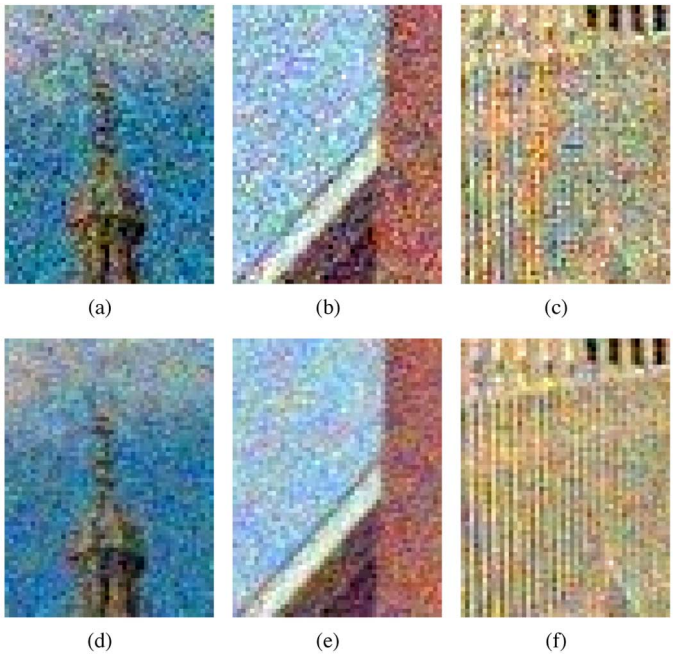

Fig. 9. Reconstruction in noise (no denoising methods applied). Top row: State-of-the-art reconstruction of Bayer sensor data in Figs. 6–8(b) under the influence of noise according to [4]. Bottom row: Optimal linear reconstruction of Pattern A sensor data in Figs. 6–8(c) under the influence of noise.

The distortion in y with respect to x_α and x_β is likewise

$$J_{x_\alpha,x_\beta} = \int_{[-\pi,\pi)^2} \frac{\gamma^2 S_{x_\ell}(\boldsymbol{\omega}) S_{x_\alpha,x_\beta}(\boldsymbol{\omega})}{S_y(\boldsymbol{\omega})} d\boldsymbol{\omega} = \frac{\gamma^2 J_{x_\ell}}{\rho^2}.$$

Differences in the number of carrier frequencies $\{\boldsymbol{\lambda}_i\}$ and the relative sizes of the weights $\{s_i, t_i\}$ render J_{x_α,x_β} less useful for comparing the performance of two distinct CFA patterns directly. However, the central role of $S_{x_\ell}(\boldsymbol{\omega}) S_{x_\alpha,x_\beta}(\boldsymbol{\omega})$ in both J_{x_α,x_β} and (9) implies that both are useful analytical tools to understand aliasing effects associated with a particular CFA.

ACKNOWLEDGMENT

The authors would like to thank T. Zickler and S. J. Gortler at Harvard University for many fruitful discussions, and B. K. Gunturk [4] and X. Li [40] for kindly providing their demosaicking code for the purpose of comparative evaluation.

REFERENCES

[1] K. Hirakawa and P. J. Wolfe, "Spatio-spectral color filter array design for enhanced image fidelity," in *Proc. IEEE Int. Conf. Image Processing*, 2007, vol. 2, pp. 81–84.

[2] D. Alleysson, S. Süsstrunk, and J. Hérault, "Linear demosaicing inspired by the human visual system," *IEEE Trans. Image Process.*, vol. 14, no. 4, pp. 439–449, Apr. 2005.

[3] E. Dubois, "Filter design for adaptive frequency-domain Bayer demosaicking," in *Proc. IEEE Int. Conf. Image Processing*, 2006, pp. 2705–2708.

[4] B. K. Gunturk, Y. Altunbasak, and R. M. Mersereau, "Color plane interpolation using alternating projections," *IEEE Trans. Image Process.*, vol. 11, no. 9, pp. 997–1013, Sep. 2002.

[5] L. Zhang and X. Wu, "Color demosaicking via directional linear minimum mean square-error estimation," *IEEE Trans. Image Process.*, vol. 14, no. 12, pp. 2167–2178, Dec. 2005.

[6] K. Hirakawa, X.-L. Meng, and P. J. Wolfe, "A framework for wavelet-based analysis and processing of color filter array images with applications to denoising and demosaicing," in *Proc. IEEE Int. Conf. Acoust. Speech Signal Processing*, 2007, vol. 1, pp. 597–600.

[7] H. Tian, B. Fowler, and A. E. Gamal, "Analysis of temporal noise in CMOS photodiode active pixel sensor," *IEEE J. Solid-State Circuits*, vol. 36, no. 1, pp. 92–101, Jan. 2001.

[8] M. Parmar and S. J. Reeves, "Selection of optimal spectral sensitivity functions for color filter arrays," in *Proc. IEEE Int. Conf. Image Processing*, 2006, vol. 3, pp. 1005–1008.

[9] B. P. Olding and R. J. Motta, "Method of defining coefficients for use in interpolating pixel values," U.S. Patent 6 970 597 B1, 2005.

[10] E. Dubois, "The sampling and reconstruction of time-varying imagery with application in video systems," *Proc. IEEE*, vol. 73, no. 4, pp. 502–522, Apr. 1985.

[11] B. E. Bayer, "Color imaging array," U.S. Patent 3 971 065, 1976.

[12] S. Yamanaka, "Solid state color camera," U.S. Patent 4 054 906, 1977.

[13] R. M. Mersereau, "The processing of hexagonally sampled two-dimensional signals," *Proc. IEEE*, vol. 67, no. 6, pp. 930–949, Jun. 1979.

[14] ICX252AK (Complimentary Color, DIP), Sony Corp., 1999 [Online]. Available: http://www.sony.net/Products/SC-HP/cx_news/vol18/pdf/icx252.pdf

[15] New Super CCD Image Sensor Significantly Improves the Color, Clarity, and Sharpness of Digial Pictures Fuji Photo Film Co., Ltd., 2000 [Online]. Available: http://home.fujifilm.com/pma2000/sprccd.html

[16] T. Yamada, K. Ikeda, Y.-G. Kim, H. Wakoh, T. Toma, T. Sakamoto, K. Ogawa, E. Okamoto, K. Masukane, K. Oda, and M. Inuiya, "A progressive scan CCD image sensor for DSC applications," *IEEE J. Solid-State Circuits*, vol. 35, no. 12, pp. 2044–2054, Dec. 2000.

[17] E. B. Gindele and A. C. Gallagher, "Sparsely sampled image sensing device with color and luminance photosites," U.S. Patent 6 476 865 B1, 2002.

[18] Realization of Natural Color Reproduction in Digital Still Cameras, Closer to the Natural Sight Perception of the Human Eye, Sony Corp., 2003 [Online]. Available: http://www.sony.net/Sony-Info/News/Press_Archive/200307/03–029E/

[19] M. Parmar and S. J. Reeves, "A perceptually based design methodology for color filter arrays," in *Proc. IEEE Intt. Conf. Acoustics, Speech Signal Processing*, 2004, vol. 3, pp. 473–476.

[20] R. Lukac and K. N. Plataniotis, "Color filter arrays: Design and performance analysis," *IEEE Trans. Consum. Electron.*, vol. 51, no. 4, pp. 1260–1267, Nov. 2005.

[21] L. Miao and H. Qi, "The design and evaluation of a generic method for generating mosaicked multispectral filter arrays," *IEEE Trans. Image Process.*, vol. 15, no. 9, pp. 2780–2791, Sep. 2006.

[22] T. Kijima, H. Nakamura, J. Compton, and J. Hamilton, "Image sensor with improved light sensitivity," U.S. Patent 20 070 177 236, Aug. 2007.

[23] B. K. Gunturk, J. Glotzbach, Y. Altunbasak, R. W. Schafer, and R. M. Mersereau, "Demosaicking: Color filter array interpolation in single chip digital cameras," *IEEE Signal Process. Mag*, vol. 22, no. 1, pp. 44–54, Jan. 2005.

[24] D. M. Coppola, H. R. Purves, A. N. McCoy, and D. Purves, "The distribution of oriented contours in the real world," *Proc. Nat. Acad. Sci. USA*, vol. 95, pp. 4002–4006, Mar. 1998.

[25] R. Kakarala and Z. Baharav, "Adaptive demosaicing with the principal vector method," *IEEE Trans. Consum. Electron.*, vol. 48, no. 4, pp. 932–937, Nov. 2002.

[26] W. Lu and Y.-P. Tan, "Color filter array demosaicking: New method and performance measures," *IEEE Trans. Image Process.*, vol. 12, no. 10, pp. 1194–1210, Oct. 2003.

[27] R. Lukac, K. N. Plataniotis, D. Hatzinakos, and M. Aleksic, "A novel cost effective demosaicing approach," *IEEE Trans. Consum. Electron.*, vol. 50, no. 1, pp. 256–261, Feb. 2004.

[28] R. Lukac and K. N. Plataniotis, "Normalized color-ratio modeling for CFA interpolation," *IEEE Trans. Consum. Electron.*, vol. 50, no. 2, pp. 737–745, May 2004.

[29] D. D. Muresan and T. W. Parks, "Adaptive principal components and image denoising," in *Proc. IEEE Int. Conf. Image Processing*, Sep. 2003, vol. 1, pp. 101–104.

[30] D. D. Muresan and T. W. Parks, "Demosaicing using optimal recovery," *IEEE Trans. Image Process.*, vol. 14, no. 2, pp. 267–278, Feb. 2005.

[31] R. Ramanath and W. E. Snyder, "Adaptive demosaicking," *J. Electron. Imag.*, vol. 12, no. 4, pp. 633–642, Oct. 2003.
[32] K. Hirakawa and T. W. Parks, "Adaptive homogeneity-directed demosaicing algorithm," *IEEE Trans. Image Process.*, vol. 14, no. 3, pp. 360–369, Mar. 2005.
[33] K. Hirakawa and T. W. Parks, "Joint demosaicing and denoising," *IEEE Trans. Image Process.*, vol. 15, no. 8, pp. 2146–2157, Aug. 2006.
[34] K. Hirakawa and X.-L. Meng, "An empirical bayes EM-wavelet unification for simultaneous denoising, interpolation, and/or demosaicing," in *Proc. IEEE Int. Conf. Image Processing*, 2006, pp. 1453–1456.
[35] R. Lukac and K. N. Plataniotis, "Universal demosaicking for imaging pipelines with an RGB color filter array," *Pattern Recognit.*, vol. 38, no. 11, pp. 2208–2212, Nov. 2005.
[36] L. Zhang, X. Wu, and D. Zhang, "Color reproduction from noisy CFA data of single sensor digital cameras," *IEEE Trans. Image Process.*, vol. 16, no. 9, pp. 2184–2197, Sep. 2007.
[37] K. Hirakawa and P. J. Wolfe, "Second-generation CFA and demosaicking design," presented at the IS&T/SPIE 19th Annu. Symp. Electronic Imaging, 2008.
[38] Spectral Database, Univ. Joensuu Color Group [Online]. Available: http://spectral.joensuu.fi
[39] Diagonal 6 mm (type 1/3) Progressive Scan CCD Image Sensor With Square Pixel for Color Cameras Sony Corp., 2004 [Online]. Available: http://products.sel.sony.com/semi/PDF/ICX204AK.pdf
[40] X. Li, "Demosaicing by successive approximation," *IEEE Trans. Image Process.*, vol. 14, no. 3, pp. 370–379, Mar. 2005.

Keigo Hirakawa (M'06) received the B.S.E. degree in electrical engineering from Princeton University, Princeton, NJ, in 2000, the M.S. and Ph.D. degrees in electrical and computer engineering from Cornell University, Ithaca, NY, in 2003 and 2005, respectively, and the M.M. degree in Jazz Performance from the New England Conservatory of Music, Boston, MA, in 2006.

He is currently with the School of Engineering and Applied Sciences and the Department of Statistics at Harvard University, where he co-leads a collaboration with Sony Electronics, Inc. He has previously been an ASIC engineer and principal image scientist for the camera division of Hewlett-Packard/Agilent Technologies, and his past and current collaborations with camera manufacturers include Sony, Micron, Texas Instruments, and NEC.

Dr. Hirakawa has received a Lockheed Martin fellowship award (2001) and a DoCoMo innovative paper award (jointly with Prof. Wolfe; IEEE ICIP 2007); he has also been selected a closing keynote speaker at IS&T CGIV 2008. His research focuses on statistical signal processing, color imaging, and computer vision.

Patrick J. Wolfe (S'96–M'03–SM'08) received the B.S. degree in electrical engineering and the B.Mus. degree concurrently from the University of Illinois at Urbana-Champaign, Urbana, in 1998, both with honors, and the Ph.D. degree in engineering from the University of Cambridge, Cambridge, U.K., as a National Science Foundation Graduate Research Fellow, working on the application of perceptual criteria to statistical audio signal processing.

Prior to founding the Statistics and Information Sciences Laboratory at Harvard University in 2004, he held a Fellowship and College Lectureship jointly in Engineering and Computer Science at New Hall, a University of Cambridge constituent college where he also served as Dean. He has also taught in the Department of Statistical Science at University College, London, U.K., and continues to act as a consultant to the professional audio community. In addition to his diverse teaching activities, he has published in the literatures of engineering, computer science, and statistics. His research group focuses on statistical signal processing and its application to tasks involving modern high-dimensional data sets, in particular images, sounds, and networks.

Dr. Wolfe has received honors from the IEEE, the Acoustical Society of America, and the International Society for Bayesian Analysis.